AGU PUBLICATIONS

Tectonics

RESEARCH ARTICLE
10.1002/2015TC004085

Key Points:
- Transtensional graben system at transition between Central Alps and its foreland studied for first time
- Links graben kinematics to formation of Western Alps arc and rollback of west Mediterranean slab
- Application of novel dating technique of fibers on fault planes

Correspondence to:
U. Ring,
uwe.ring@geo.su.se

Citation:
Ring, U., and A. Gerdes (2016), Kinematics of the Alpenrhein-Bodensee graben system in the Central Alps: Oligocene/Miocene transtension due to formation of the Western Alps arc, *Tectonics*, *35*, doi:10.1002/2015TC004085.

Received 18 NOV 2015
Accepted 20 MAR 2016
Accepted article online 31 MAR 2016

Kinematics of the Alpenrhein-Bodensee graben system in the Central Alps: Oligocene/Miocene transtension due to formation of the Western Alps arc

Uwe Ring[1] and Axel Gerdes[2]

[1]Institutionen för geologiska vetenskaper, Stockholms universitet, Stockholm, Sweden, [2]Institut für Geowissenschaften, Goethe-Universität, Frankfurt, Germany

Abstract We report fault slip data from exhumed fault surfaces along the NNE trending Alpenrhein valley and its intersection with the WNW striking Bodensee Graben near the Alpine thrust front of the Central Alps in the Swiss-Austrian-German border region. This conjugated graben system straddles the boundary between the Alps and its foreland and allows comparing the kinematics of graben formation between the two different tectonic domains. Our data show sinistral transtension along the Alpenrhein Graben and dextral transtension along the Bodensee Graben. Both transtensional graben systems resulted from the same kinematic regime of NW directed shortening and NE oriented extension. The graben faults are not older than NW striking tear faults associated with NW directed Oligocene nappe emplacement in the Helvetics starting at 35–30 Ma and ending by 25–20 Ma. Compatible with this are six U-Pb ages of calcite fibers from four samples yielding consistent ages ranging from 25.3 ± 5.6 Ma to 21.8 ± 3.4 Ma (2σ errors). Earthquake data since 1996 show that kinematic directions persisted until the Recent. Our data broadly fit with the kinematic evolution of the Oberrhein Graben, which shows significant E-W extension in the Oligocene. We suggest that Oligocene extension in the Alps and its foreland resulted from the increased curvature of the Western Alps arc and associated moderate tangential stretching in the internal parts of the Central Alps. We discuss a tectonic model of eastward rollback of the west Mediterranean subduction zone associated with counterclockwise rotation of Adria, the latter of which aided the formation of the Western Alps arc.

1. Introduction

The tectonic evolution of extensional/transtensional graben systems in the forelands of compressive orogens and their tectonic and temporal relation to ductile extension and graben formation within the orogen remains a tectonic problem. Central to the understanding of how the foreland graben systems form and develop is their kinematics and timing with respect to major evolutionary steps in the developing compressive orogen.

There are a number of driving forces for horizontal extension in the high-grade internides of orogens [*Platt*, 1986; *Houseman and England*, 1986; *Royden*, 1993; *Molnar*, 2015], but relating one of these steering mechanisms to the actual extension structures is not straightforward and a matter of controversy. In the highly metamorphosed internal parts of the Central Alps there is evidence for limited tangential (E-W) stretching in the Oligocene and Miocene [*Mancktelow*, 1985; *Merle et al*., 1989; *Ring*, 1992, 1994; *Nievergelt et al*., 1996; *Steck*, 2008; *Ciancaleoni and Marquer*, 2008]. In the frontal, weakly metamorphosed parts of the Central Alps, no E-W horizontal extension has been reported, but there is evidence for Oligocene/Miocene graben formation in the direct foreland of the Alps (Oberrhein and Bonndorf-Bodensee graben systems, Figure 1). Being able to temporally link E-W horizontal extension from the internal via the external parts of the Central Alps into their foreland may help to define a plausible driving mechanism for tangential extension.

In the foreland of the Alps, the European Cenozoic Rift System (ECRIS) developed since the Eocene [*Illies*, 1975; *Illies and Greiner*, 1978; *Ziegler*, 1994]. ECRIS mainly consists of the Oberrhein, the Limagne (or Massif Central), and the Bresse-Rhône graben systems and their prolongation into the west Mediterranean (Figure 1). The opening of the Oberrhein Graben in the Eocene was due to sinistral strike-slip deformation resulting from north directed shortening [*Bergerat*, 1987; *Schumacher*, 2002]. A major kinematic change took place in the Oligocene between ~34 and 28 Ma when the main extension phase associated with vertical shortening and E-W oriented extension took place [*Illies*, 1978; *Bergerat*, 1987; *Schumacher*, 2002]. Another significant change in the early Miocene was the shift to horizontal NW shortening, while extension remained horizontal in the NE direction [*Bergerat*, 1987; *Lacombe et al*., 1993; *Schumacher*, 2002]. This kinematic regime caused renewed sinistral

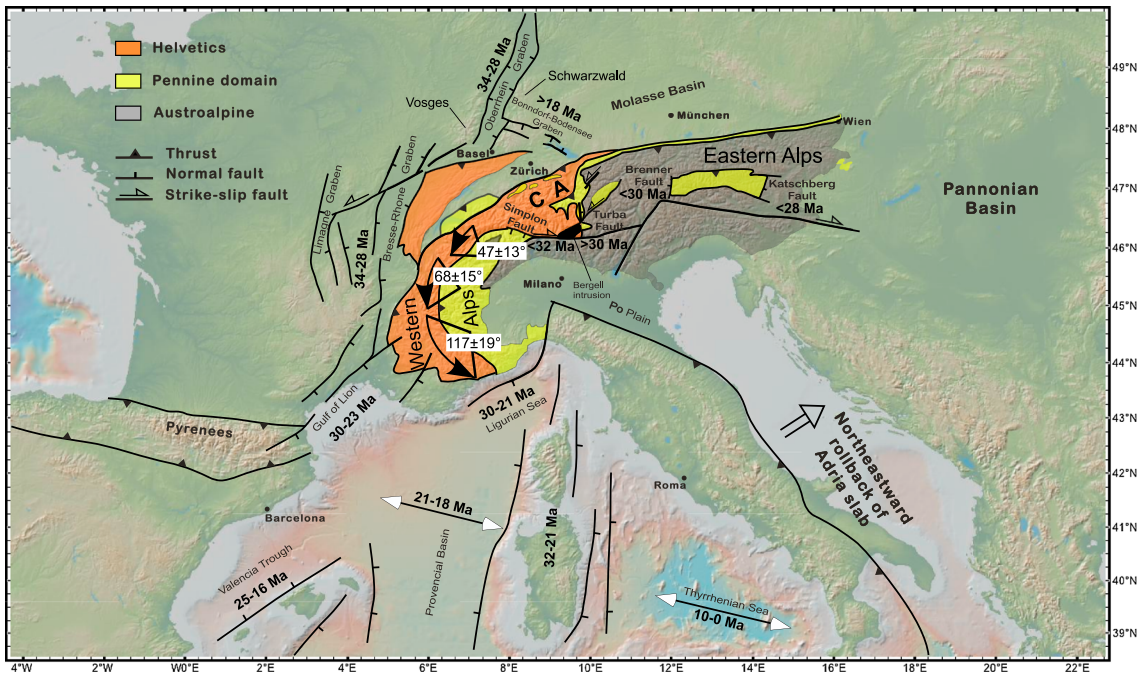

Figure 1. Overview relief map of southwest and central Europe with main tectonic units of Alps (CA = Central Alps), major graben structures of European Cenozoic Rift System (ECRIS), opening directions of west Mediterranean basins, and paleomagnetically derived rotation angles in Western Alps [*Thomas et al*., 1999; *Collombet et al*., 2002]. Age data for formation and activity of major extension in ECRIS, Alps, and west Mediterranean summarized from *Bergerat* [1987], *Nievergelt et al*. [1996], *Lonergan and White* [1997], *Schumacher* [2002], *Rosenbaum et al*. [2002], *Michon et al*. [2003], *Steck* [2008], and *Glodny et al*. [2008].

strike-slip faulting, was associated with shortening and regional uplift since ~21 Ma, and persists to the present [*Ahorner*, 1975; *Müller et al*., 1997; *Plenefisch and Bonjer*, 1997]. This is shown, for instance, in the southernmost Oberrhein Graben and the Bresse-Rhein transfer zone where ENE trending folds affecting Late Pliocene alluvial deposits formed coevally with left-lateral strike-slip along NNE trending faults [*Giamboni et al*., 2004; *Ustaszewski and Schmid*, 2007]. These structures reflect the interplay between NW directed shortening in the Alps/Jura and graben tectonics in the foreland.

The rest of ECRIS underwent a largely similar tectonic history with late Eocene transtensional kinematics and an Oligocene main extensional stage typical for ECRIS [*Ziegler*, 1994; *Sissingh*, 1998; *Michon et al*., 2003] (Figure 1). The pure extensional kinematics remained active until the late Aquitanian (21.5 Ma) when the oceanic Provençal Basin began to open at the southern end of ECRIS due to ongoing eastward rollback of the west Mediterranean subduction zone. Burdigalian (20.5–16 Ma) sediments represent the latest synrift deposits in southern ECRIS [*Merle et al*., 1998; *Michon and Merle*, 2001; *Sissingh*, 2001].

In general, the tectonic evolution of ECRIS since the Eocene is related to major tectonic events in the Alpine and Pyrenean collision zones [*Illies*, 1978]. Most workers seem to agree that the formation of ECRIS in the Eocene was by collisional foreland splitting [*Sengör*, 1976; *Sengör et al*., 1978; *Illies and Greiner*, 1978; *Dezes et al*., 2004]. *Séranne* [1999], *Roca et al*. [1999], and *Lacombe and Jolivet* [2005] showed that the southern sectors of ECRIS (Gulf of Lion, Valencia Trough) were controlled by back-arc extension related to rollback of the west Mediterranean trench since the Oligocene (35–30 Ma), a time when ECRIS underwent its main extension phase. *Dezes et al*. [2004] related the kinematic change in the early Miocene to reorientation of the stress field in the Alpine foreland due to the decay of compressional stresses in the Pyrenean collision zone and the onset of seafloor spreading in the Provençal Basin. This kinematic change explains why the Limagne and Bresse-Rhône Graben became inactive [*Michon and Merle*, 2001], while the Oberrhein Graben remained active until the present.

The connection of ECRIS with subduction zone rollback in the west Mediterranean has already been mentioned. The rollback of the west Mediterranean subduction zone and the sequential opening of the west Mediterranean basins has first been proposed by *Lonergan and White* [1997] and basically follows *Carey* [1958], who showed that the unbending of the arcuate mountain belts in the west Mediterranean results

in a relatively straight E-W oriented assembly of Iberia, the Balearic islands, Corsica, Sardinia, Sicily, and Italy with the Pyrenees and the Alps. The opening of the Ligurian Sea with displacement of the Corsica-Sardinia block during the Oligocene had a strong influence on the Alpine arc [*Rosenbaum et al*., 2002], a feature also shown in the reconstruction by *van Hinsbergen et al*. [2014]. Rollback resulted in the oceanization of the Provençal Basin at 21.5 Ma [*Carminati et al*., 1998].

The increased curvature of the Western Alps arc has been by documented by analysis of kinematic indicators [*Gidon*, 1974; *Vialon et al*., 1989] and quantified by paleomagnetic data, the latter of which indicate large systematic and regional counterclockwise rotations [*Heller*, 1980; *Thomas et al*., 1999; *Collombet et al*., 2002] (Figure 1). Post-Eocene kinematic indicators show right-lateral slip along longitudinal faults and counterclockwise rotation of transport directions along the Western Alpine arc and were interpreted to have resulted from regional counterclockwise rotation of the Western Alps [*Gidon*, 1974; *Vialon et al*., 1989]. The amount of counterclockwise rotation increases significantly and consistently from north to south, with $47 \pm 13°$ rotation in the north [*Thomas et al*., 1999], $68 \pm 15°$ in the central part, and $117 \pm 19°$ in the southernmost parts of the Western Alps [*Collombet et al*., 2002] (Figure 1). *Maffione et al*. [2008] proposed that rollback of the west Mediterranean subduction zone and the associated rotation of Corsica and Sardinia aided the formation of the Western Alps arc.

The aim of this contribution is to constrain the kinematics and timing of the Alpenrhein Graben and its junction with the Bodensee Graben at the Alpine deformation front in the Swiss-Austrian-German border region. We then relate graben formation to E-W extension in the internal Central Alps and the ECRIS graben in the direct foreland of the Alps. Finally, we discuss a tectonic model linking subduction zone rollback in the west Mediterranean with extension across ECRIS and tangential stretching in the Central Alps.

2. Setting

2.1. Alps

The Alps are the result of Adria-Europe convergence in the Cretaceous and Tertiary and consist of the Austroalpine (part of Adria, upper plate), the partly oceanic Pennine domain, and the Helvetics (southern edge of Europe, lower plate) [*Schmid et al*., 2004] (Figure 1). Since the Eocene, nappe stacking, high-pressure metamorphism, and orogenic development is due to NW directed convergence between Adria and Europe. The counterclockwise rotation of Adria since the Oligocene is a major factor in the formation of the present-day structure of the Alps [*Dewey et al*., 1989; *Laubscher*, 1991; *Platt et al*., 1993]. This rotation is still ongoing around a pole close to Milano [*Calais et al*., 2002], explains the predominance of right-lateral motion observed around the Alps, and controlled indentation tectonics of Adria in the Eastern and Central Alps [*Ratschbacher et al*., 1991; *Schmid et al*., 2004].

In the Oligocene at ~34–30 Ma, the Central and Eastern Alps started extending in the E-W direction parallel to the belt [*Ring*, 1994; *Nievergelt et al*., 1996; *Challandes et al*., 2003; *Glodny et al*., 2008; *Steck*, 2008]. Extension in the internal parts was initially accommodated by low-angle faults, which were cut by high-angle normal faults. The amount of extension was rather limited; only in the eastern Tauern Window and to the east of it, Miocene extension occurred at a large scale [*Ratschbacher et al*., 1991]. It appears that E-W extension is limited to the internal parts of the Alps and was coeval with ongoing NW directed shortening [*Ring*, 1994; *Nievergelt et al*., 1996; *Glodny et al*., 2008; *Steck*, 2008]. This is shown, for instance, in the Helvetic nappes, which had their main phase of nappe transport at 35–30 Ma with movement continuing until 25–20 Ma [*Hunziker et al*., 1986]. *Sue and Tricart* [2002] suggested that extension in the internal parts of the Western Alps also commenced in the Oligocene.

An interesting and not understood geometric feature is the drastic thinning of the Helvetics across the Alpenrhein valley [*Oberhauser*, 1965] (Figures 1–3). Because of the markedly reduced Helvetic nappe pile and the large areal outcrop of the Pennine and Austroalpine units east of the Alpenrhein valley (Figure 3), the cause for that thinning appears to be syntectonic to posttectonic. The Alpenrhein valley may thus represent an exceptional Tertiary graben near the Alpine thrust front, which we name Alpenrhein Graben.

To the north near Bregenz, the Alpenrhein Graben joins with the Bodensee Graben (Figures 1 and 2) thus providing a unique opportunity to compare possible graben formation within the Alps with that in its foreland and via the Bonndorf Graben with the Oberrhein Graben. The Bonndorf-Bodensee graben system

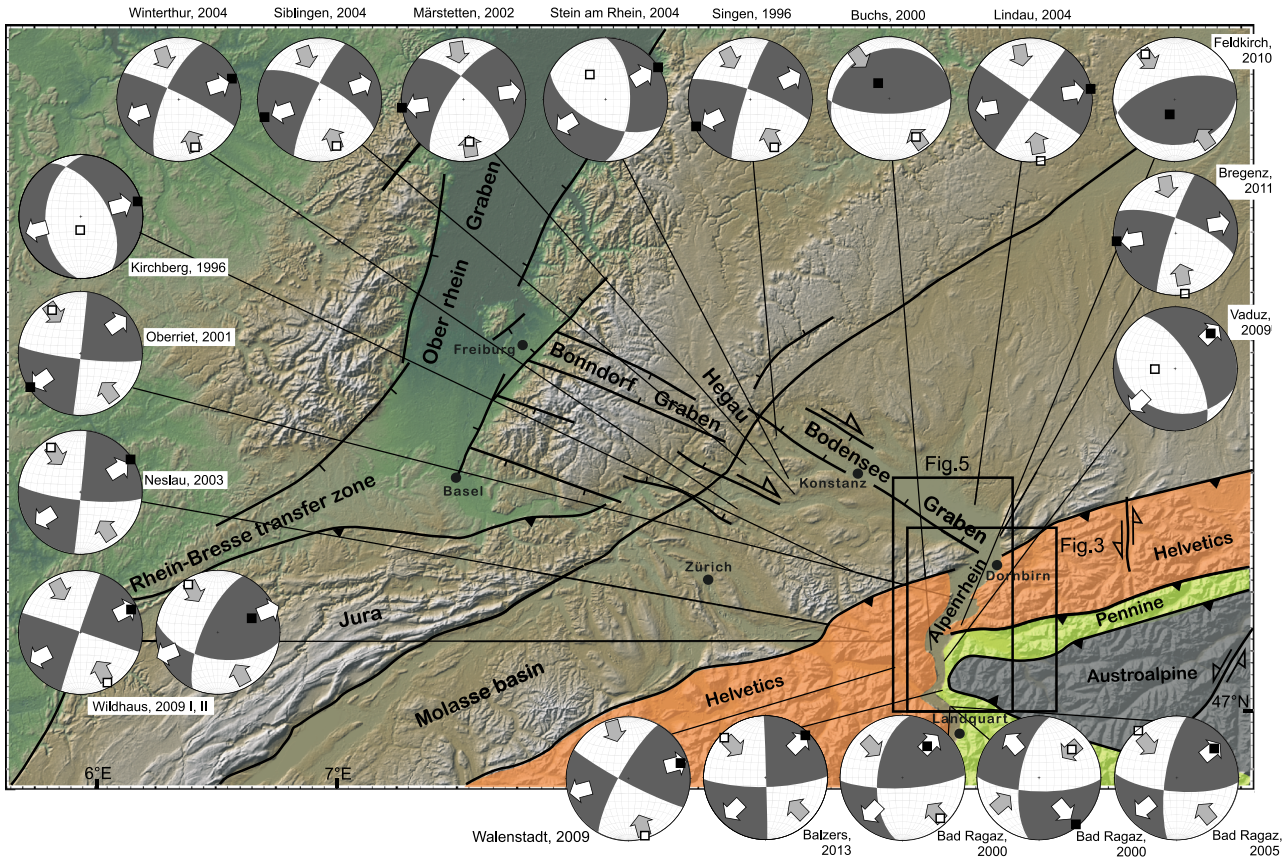

Figure 2. Relief map of northern Central Alps and foreland with main tectonic units; note large-scale synclinal position of Austroalpine unit east of Alpenrhein valley and lack of this structure west of Alpenrhein (note geographical distinction between Oberrhein (Upper Rhine) north of Basel and Alpenrhein (Alpine Rhine) south of Dornbirn). Focal plane solutions of $M > 3$ earthquakes in wider Alpenrhein region since 1996 (http://www.seismo.ethz.ch) are also shown (shortening: open quadrangle, grey arrow; extension: black quadrangle, open arrow; town near which earthquake occurred and year are indicated); most earthquakes are strike-slip events resulting from NW shortening and NE extension; in addition three normal fault (Kirchberg, Stein am Rhein, and Vaduz) and two thrust earthquakes (Buchs and Feldkirch) occurred; all data, except Bad Ragaz, 2000, show either horizontal NE directed extension or horizontal NW directed shortening or both.

formed >18 Ma due to dextral transtension and reactivation of WNW striking Carboniferous faults [*Schreiner*, 1975, 1979; *Hofmann et al*., 2000]. Graben development was accompanied by the 16–8 Ma old Hegau volcanics [*Keller*, 1984].

2.2. Subduction Zone Rollback in West Mediterranean and Extension in Alps

The rollback of the west Mediterranean subduction zone reshaped the Alps-Pyrenees orogenic belt by tearing it apart and displacing and rotating parts of it [*Argand*, 1924; *Carey*, 1958; *Lonergan and White*, 1997; *Rosenbaum et al*., 2002; *Faccenna et al*., 2004; *van Hinsbergen et al*., 2014]. Rollback began in the early Oligocene (35–30 Ma) and is still ongoing [*Royden*, 1993] (Figure 1). It opened the west Mediterranean basins and displaced and rotated, for instance, the Balearic islands, Calabria, Sardinia, Corsica, and present-day Italy considerably. *Faccenna et al*. [2004], showed that in the Liguro-Provençal and Tyrrhenian region (Figure 1), extension was of the order of ~780 km. The rate of extension was on average 2.6 cm/a with a pause between 15 and 10 Ma, when the velocity of rollback drastically decreased. As a result of retreat and associated large-scale extension, Adria underwent counterclockwise rotation of the order of 40–50° since ~35 Ma [*Lowrie and Alvarez*, 1975; *Dewey et al*., 1989; *Rosenbaum et al*., 2002]. As mentioned above, the rotation of Adria played a key role in mountain building processes in the Alps [*Channell et al*., 1979; *Dewey et al*., 1989; *Platt et al*., 1993].

Champagnac et al. [2006] proposed that orogen-parallel extension in the Western Alps is related to the opening of the Ligurian Sea and therefore to rollback of the west Mediterranean trench. The opening of the Ligurian Sea is supposed to be a free boundary for the development of a lateral extrusion system. The

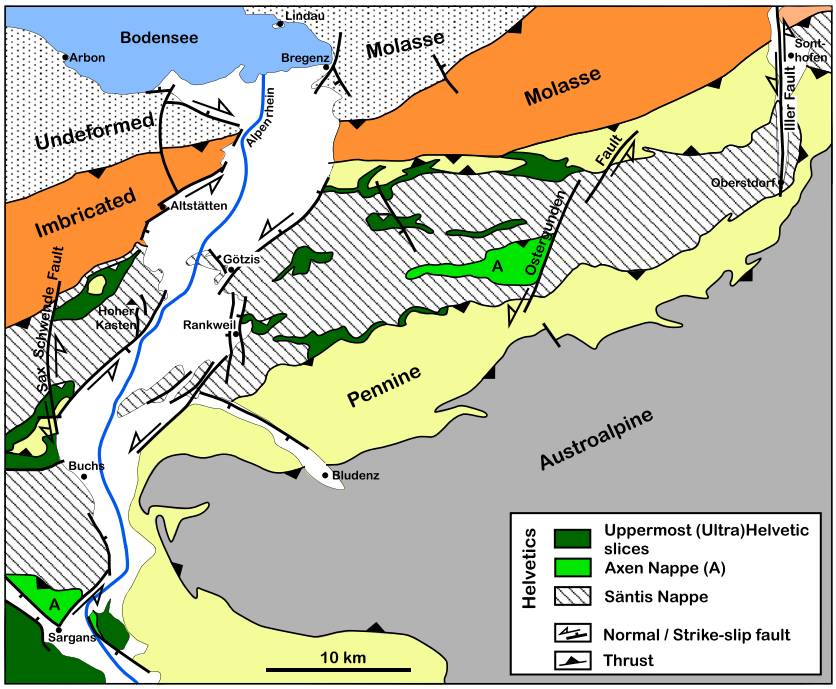

Figure 3. Simplified tectonic map of Alpine nappe stack across Alpenrhein Graben; map modified and simplified from 1:200,000 map of Vorarlberg [*Oberhauser and Rataj*, 1998; *Ortner et al*., 2015; *Sala et al*., 2014; *Pomella et al*., 2015]; refer to Figure 2 for location of map. Nappe contacts west of Alpenrhein Graben are south dipping; geology east of Alpenrhein valley is characterized by large-wavelength syncline/anticline pair cored by Austroalpine and Helevtic Säntis Nappe; Säntis Nappe shows drastic change in outcrop pattern across Alpenrhein Graben with apparent sinistral offset; note also sinistral faults in vicinity of Alpenrhein Graben (Iller Fault, Ostergunden fault system, Sax-Schwende Fault); contacts of imbricated Molasse with Säntis Nappe above and undeformed Molasse below are hardly offset.

Ligurian-Provençal Basin started to extend at ~32–31 Ma, as indicated by synrift sediments that occur both onshore and offshore at the northern Ligurian (Provençal) margin [*Bellaiche et al*., 1976], in the Gulf of Lion [*Séranne*, 1999], and in the Sardinian rift [*Cherchi and Montadert*, 1982] and also fission-track thermochronology in Corsica [*Zarki-Jakni et al*., 2004]. The timing derived from fission-track dating for the onset of rapid rift-related denudation is consistent with results from other basement massifs surrounding the Ligurian-Provençal basin, e.g., the Maures-Tanneron Massif [*Morillon*, 1997] and the eastern Pyrenees [*Maurel et al*., 2002].

The counterclockwise rotation of Adria since the early Oligocene is a major factor in the formation of the Alpine arc [*Gidon*, 1974; *Ménard*, 1988; *Collombet et al*., 2002]. Here we argue that west Mediterranean rollback not only had an influence on the Alpine arc but also on tangential stretching in the Central Alps, the Alpenrhein-Bodensee graben system, and the main rifting stage of ECRIS in the Oligocene.

2.3. Geology Across the Alpenrhein Graben

Alpine geology and the architecture of the nappe pile changes across the Alpenrhein Graben (Figures 2 and 3), which is in part due to an easterly plunge of major tectonic axes in the eastern Central Alps. The main tectonic unit in the region is the Säntis Nappe, the most frontal Helvetic nappe in the area. West of the Alpenrhein Graben, the Säntis Nappe crops out over a rather huge area, and the outcrop width in N-S is ~22–25 km. The architecture of the nappe stack is relatively simple with south dipping nappe contacts. East of the Alpenrhein Graben, the geology is dominated by a large-wavelength syncline cored by the Austroalpine unit and an anticline cored by the Säntis nappe (Figure 3) (see also cross sections by *Pomella et al*. [2015] and *Ortner et al*. [2015]). The outcrop width of the Säntis Nappe in N-S is $<$14 km, and higher parts of the nappe stack (Axen Nappe and (ultra)Helvetic slices) are exposed [*Oberhauser*, 1965; *Pomella et al*., 2015] (Figure 3).

The outcrop pattern of the Säntis Nappe in map view suggests a component of sinistral displacement across the Alpenrhein valley (Figure 3). Accordingly, a steeply southeast dipping fault ("Emsrütti Bruch") along the Alpenrhein Graben near Dornbirn has been proposed by *Oberhauser* [2005]. There is more evidence for

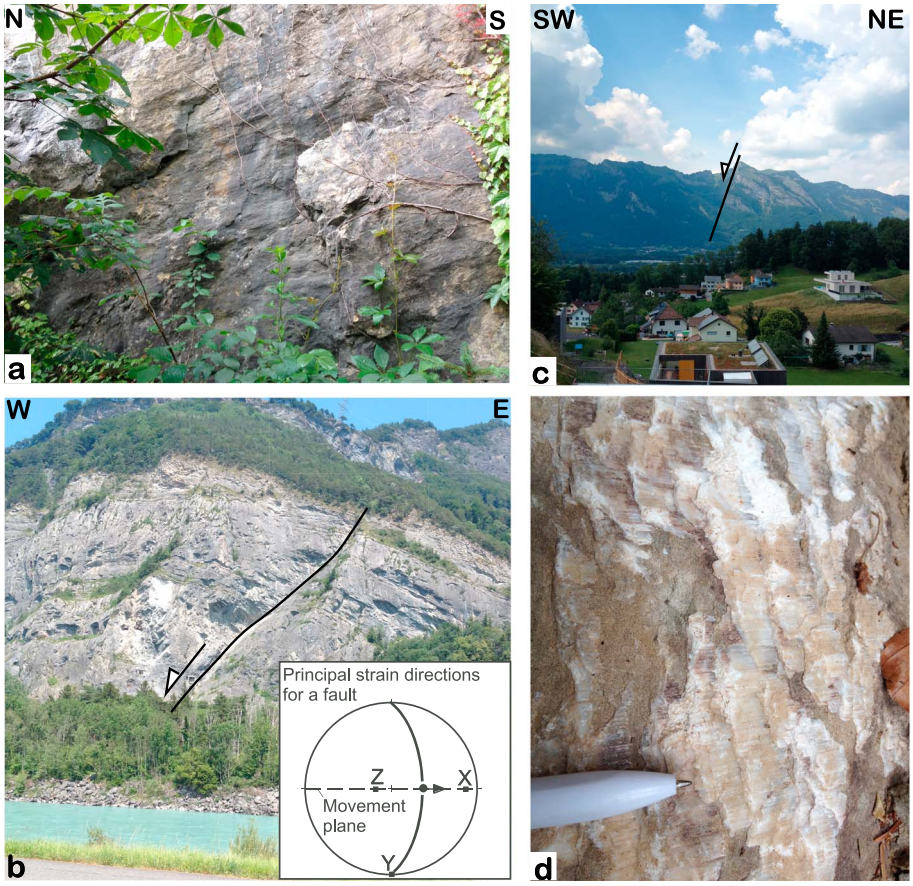

Figure 4. Outcrop photos of faults and fault structures; refer to Figure 5 for localities. (a) N-S striking, near vertical, sinistral fault just east of bridge over Fruz river in Rankweil (outcrop Fr15 in Figure 5); striations plunging at 20°N. (b) SW dipping normal fault with striations plunging toward 230°; east of Sargans. (c) SW dipping normal fault at Hoher Kasten, west of Sennwald. (d) Calcite fibers indicating dextral movement on fault plane in sandstone (Altmannschichten) west of Eichberg. Inset: graphical construction of principal incremental shortening and extension axes for given fault; movement plane of fault perpendicular to fault plane containing unit vector parallel to direction of accumulated slip and normal vector to fault plane; shortening and extension axes at 45° to fault plane.

sinistral faulting along NE and north striking faults, for instance, the Sax-Schwende Fault, the Ostergunden fault system, and the Iller Fault (Figure 3). Across the Iller Fault near Sonthofen/Oberstdorf, the hinge of the Säntis Nappe-cored anticline is plunging east, and east of the Iller Fault the Säntis Nappe is displaced to the north. However, east of the Iller Fault the Pennine unit is not outcropping above/north of the Säntis Nappe anymore (Figure 3). Therefore, sinistral faulting occurred during large-scale folding and emplacement of the folded Pennine/Helvetics stack upon the imbricated Molasse. Furthermore, *Bertle* [1970] reported a NE striking sinistral strike-slip fault farther east (Figure 2). All these faults strike N/NE and are at a high angle to well-known tear faults in the Helvetic Nappes [*Oberhauser and Rataj*, 1998; *Funk et al*., 2000].

Because higher parts of the Alpine nappe stack are exposed east of the Alpenrhein, it also appears that the east block has been downfaulted. However, deformed Molasse and its thrust contacts with the Säntis Nappe above and undeformed Molasse below are hardly offset by any faulting [see *Funk et al*., 2000]. At the northern front of the Alps, these contacts are supposed to be post middle Miocene (<12 Ma) in age [*Funk et al*., 2000].

Since the early Pleistocene, up to eight glaciations at the Alpine front and the Bodensee area have been proposed [*Ellwanger et al*., 2011; *Preusser et al*., 2011]. Glacial abrasion of fault surfaces and postglacial backfill of the Alpenrhein valley altered the fault structures and their exposure. The Alpenrhein valley can be regarded as a polygenetic fluvioglacial landform in which the glacial processes modified an earlier tectonic and fluviatile valley.

Table 1. Fault Slip Data

Locality	Latitude/Longitude	Unit	Extension Axes (With Eigenvalue)	Intermediate Axes (With Eigenvalue)	Shortening Axes (With Eigenvalue)
Alt3	47°25′25″N, 9°35′22″E	Untere Süßwassermolasse	14/28 (−0.4639)	204/62 (0.0050)	106/4 (0.4590)
Au2	47°26′45″N, 9°38′06″E	Untere Meeresmolasse	260/26 (−0.3614)	132/51 (0.0960)	4/27 (0.2654)
Daf13	47°17′31″N, 9°40′06″E	Vorarlberger Flysch	251/74 (−0.3084)	84/16 (0.0158)	353/3 (0.2926)
Dü16	47°15′12″N, 9°38′41″E	Schrattenkalk	265/32 (−0.3185)	90/58 (−0.0463)	356/2 (0.3648)
Egg4	47°20′18″N, 9°30′38″E	Untere Meeresmolasse	59/23 (−0.2339)	262/66 (−0.0911)	152/9 (0.3350)
Fl21	47°05′09″N, 9°20′32″E	Verrucano	40/9 (−0.3788)	308/16 (−0.0291)	159/72 (0.4079)
Fr15	47°16′31″N, 9°39′35″E	Schrattenkalk	229/3 (−0.2862)	132/69 (−0.0242)	320/21 (0.3105)
Ga10	47°13′27″N, 9°31′31″E	Schrattenkalk	232/19 (−0.1899)	81/68 (−0.0971)	326/9 (0.2870)
Gö12	47°19′31″N, 9°38′21″E	Schrattenkalk	303/20 (−0.4402)	183/54 (0.0196)	44/29 (0.4206)
Hoh11	47°22′51″N, 9°43′00″E	Schrattenkalk	281/31 (−0.3171)	41/40 (−0.0957)	167/35 (0.4128)
Kr5	47°19′40″N, 9°32′52″E	Seewenkalk	25/70 (−0.1839)	264/11 (−0.0497)	171/17 (0.2336)
La14	47°16′07″N, 9°40′47″E	Schrattenkalk	83/59 (−0.3423)	239/29 (0.0201)	335/11 (0.3222)
Me19	47°04′39″N, 9°23′30″E	Melser Sandstein	225/11 (−0.4860)	315/1 (−0.0041)	48/79 (0.4901)
Neu8	47°17′33″N, 9°31′26″E	Schrattenkalk	98/15 (−0.3939)	197/30 (0.0368)	345/55 (0.3571)
Ob6	47°18′52″N, 9°33′01″E	Schrattenkalk	256/64 (−0.4917)	18/15 (0.0002)	114/21 (0.4916)
Pf1	47°29′18″N, 9°45′59″E	Nagelfluh	255/9 (−0.4716)	337/4 (0.0040)	77/66 (0.4676)
Rh26	47°22′31″N, 9°36′17″E	Untere Meeresmolasse	44/10 (−0.2965)	304/48 (0.1241)	143/41 (0.1939)
Ro28	47°28′26″N, 9°32′14″E	Obere Meeresmolasse	234/1 (−0.2285)	144/25 (0.0346)	326/65 (0.1940)
Rü7	47°18′18″N, 9°32′52″E	Schrattenkalk	68/26 (−0.3862)	204/56 (−0.0818)	328/21 (0.4680)
Ru22	47°03′40″N, 9°23′28″E	Verrucano	38/8 (−0.3100)	307/11 (0.0126)	145/78 (0.2974)
Sa17	47°11′51″N, 9°42′22″E	Vorarlberger Flysch	20/1 (−0.4584)	110/18 (−0.0131)	286/72 (0.4715)
Sa18	47°02′58″N, 9°26′18″E	Quinterkalk	241/9 (−0.3162)	149/10 (−0.0380)	10/77 (0.3542)
Sa23	47°02′30″N, 9°29′18″E	Quinterkalk	231/16 (−0.4893)	322/2 (−0.0034)	60/74 (0.4927)
Sb9	47°17′31″N, 9°40′06″E	Seewerkalk	322/40 (−0.3430)	159/49 (0.0362)	59/9 (0.3068)
Th27	47°14′03″N, 9°32′13″E	Obere Meeresmolasse	83/49 (−0.1954)	267/49 (−0.1461)	175/2 (0.3415)
Tr24	47°04′05″N, 9°28′14″E	Schrattenkalk	202/5 (−0.2026)	295/26 (0.0818)	101/64 (0.1208)
Wal20	47°06′57″N, 9°18′10″E	Eisensandstein	54/8 (−0.3645)	196/80 (−0.0077)	323/7 (0.3722)

3. Methods

3.1. Fault Slip Analysis

To evaluate fault kinematics, the orientation of primary and secondary fault planes, the trend and plunge of striations, and the sense of relative displacement on these planes have been mapped. In this study a simple graphical method is applied to determine principal strain axes using the program "Fault Kinematics" written by Rick Allmendinger [*Marrett and Allmendinger*, 1990; *Allmendinger et al*., 2012]. The method graphically constructs the principal incremental shortening and extension axes for a given population of faults. Each pair of axes lies in the movement plane of the fault (a plane perpendicular to the fault plane that contains the unit vector parallel to the direction of accumulated slip and the normal vector to the fault plane). Furthermore, each pair of axes is at an angle of 45° to each of the vectors (Figure 4, inset). To distinguish between the shortening and extension axes, it is necessary to have information on the sense of slip, which has been deduced from the orientation of fibers, striae, and fractures associated with the fault (Figure 4) [*Hancock*, 1985; *Petit*, 1987]. Fiber and striae orientations on slickensides from the subsidiary faults in the Alpenrhein Graben are usually simple and consistent and are readily interpretable with the geometry of the mapped faults at a regional scale.

Marrett and Allmendinger [1990] proposed that the brittle deformation in a faulted region can be directly related to the geometric moment, which may be expressed as the product of the average displacement and the fault surface area. This approach requires weighting the fault slip data with the displacement and the fault surface area. Once the moment tensors are summed, strain magnitudes can be calculated. However, we have no information about slip magnitudes and fault surface area. Therefore, we can only determine the orientations (eigenvectors) of the principal strain axes. The absolute magnitudes (eigenvalues) cannot be calculated. The eigenvalues reported in Table 1 are normalized and a proxy of the strain symmetry (see *Ring* [2008] for fuller description). Bingham distribution statistics for axial data are used to optimize clusters of kinematic axes of a fault array [*Mardia*, 1972]. The linked Bingham distribution is equivalent to an unweighted moment tensor summation (a moment tensor sum in which all faults are weighted equally).

Table 2. LA-ICP-MS U-Th-Pb Isotope Data of Calcite Fibers[a]

Spot	Sample ID	^{207}Pb[b] (c/s)	U[c] (ppb)	Pb[c] (ppb)	$\frac{Th}{U}$[c]	$\frac{^{238}U}{^{206}Pb}$	±2σ (%)	$\frac{^{207}Pb}{^{206}Pb}$	±2σ (%)
seq 1									
A06	H6	9,903	145	137	0.02	1.772	1.5	0.8413	0.94
A07		14,141	282	127	0.03	3.706	1.6	0.8352	0.66
A08		24,109	126	570	0.02	0.364	1.3	0.8512	0.87
A09		10,350	232	69	0.02	5.708	1.4	0.8368	0.98
A10		16,021	202	186	0.05	1.808	2.2	0.8442	0.77
A12		21,308	220	76	0.03	5.230	1.2	0.8297	0.71
A13		17,661	153	65	0.29	4.401	1.8	0.8391	0.85
A14		10,402	87	76	0.07	1.991	1.1	0.8416	0.83
A15		27,840	72	143	0.44	0.8897	2.2	0.8454	0.95
A16		16,600	228	116	0.12	3.426	2.8	0.8401	0.79
A17		13,574	295	83	0.01	6.242	1.5	0.8292	0.89
A18		16,471	177	79	0.02	4.088	1.2	0.8430	0.99
A19		13,593	204	65	0.09	5.634	1.1	0.8326	0.82
A20		160,595	40	1109	0.49	0.0635	2.9	0.8491	0.61
A21		16,824	223	79	0.10	5.230	1.2	0.8318	0.78
A22		14,351	254	82	0.04	5.501	1.5	0.8363	0.77
A23		18,442	112	89	0.09	2.228	2.1	0.8433	0.69
A24		16,104	111	147	0.10	1.271	1.5	0.8429	1.00
A25		202,524	64	1220	0.86	0.0944	1.7	0.8497	0.58
A26		78,483	117	374	0.09	0.6028	1.2	0.8478	0.56
A27		48,012	110	79	0.06	3.454	1.6	0.8446	1.00
A28		99,684	72	709	0.17	0.1768	1.4	0.8456	0.55
A29		27,544	96	93	0.04	1.984	2.1	0.8338	0.71
A30		14,277	327	81	0.03	6.906	3.6	0.8270	0.80
A31		31,191	102	531	0.02	0.3175	2.3	0.8460	0.58
A32	H2	76,820	137	678	0.18	2.230	1.8	0.7768	0.51
A38		44,183	119	497	0.20	1.135	3.1	0.7781	0.51
A39		130,791	31	1552	1.00	0.0844	1.9	0.7812	0.49
A40		65,553	187	651	0.09	1.889	1.9	0.7733	0.61
A41		131,362	34	3990	0.90	0.0174	2.2	0.7841	0.37
A42		85,486	99	1397	0.19	0.2031	1.6	0.7784	0.48
A43		120,953	64	1097	0.45	0.5328	1.6	0.7792	0.43
A44		97,161	96	857	0.28	1.345	1.6	0.7764	0.43
A45		10,463	219	186	0.02	3.143	1.2	0.7704	1.00
A46		84,400	182	771	0.19	2.537	2.0	0.7753	0.59
A47		83,223	101	717	0.28	1.752	2.1	0.7774	0.53
A48		54,310	56	475	0.26	1.436	3.0	0.7749	0.65
A49		20,090	114	255	0.10	1.693	1.6	0.7772	0.65
A51		70,772	27	1862	0.56	0.0315	2.2	0.7834	0.50
A52		14,993	76	237	0.06	0.9862	2.5	0.7784	0.69
A53		18,447	193	395	0.02	1.160	2.3	0.7755	0.62
A54		132,951	197	1136	0.15	2.514	1.1	0.7744	0.49
A55		42,410	96	588	0.09	0.564	1.6	0.7800	0.57
A56		34,757	169	366	0.04	2.603	1.2	0.7766	0.60
A57		27,934	186	312	0.13	2.879	1.9	0.7730	0.58
A58		67,439	212	726	0.11	1.548	1.1	0.7787	0.61
A59		27,062	215	303	0.06	3.522	1.3	0.7740	0.56
A60		37,307	69	345	0.16	1.714	0.9	0.7766	0.56
A61		34,800	143	692	0.03	0.518	0.9	0.7803	0.73
A62		70,845	73	1600	0.40	0.1059	1.1	0.7816	0.49
A63		36,790	26	292	0.57	3.733	1.9	0.7712	0.55
Zechstein Dolomite, Gypsum pit, Tettenborn, Germany									
A281	ZD	15,043	2589	418	0.06	14.89	1.1	0.3588	1.7
A282	ZD	65,250	2581	1076	0.06	6.649	3.7	0.6360	2.7
A288	ZD	256,758	2171	4643	0.06	1.998	7.0	0.7943	6.2
A289	ZD	12,671	2584	299	0.06	16.63	3.6	0.2993	4.0
A290	ZD	18,798	3115	486	0.05	15.23	4.6	0.3608	5.0
A291	ZD	16,550	2719	506	0.05	15.98	2.7	0.3180	4.8
A292	ZD	11,428	2782	344	0.05	16.11	2.6	0.3048	4.8

Table 2. (continued)

Spot	Sample ID	$^{207}Pb^{b}$ (c/s)	U^{c} (ppb)	Pb^{c} (ppb)	$\frac{Th}{U}^{c}$	$\frac{^{238}U}{^{206}Pb}$	±2σ (%)	$\frac{^{207}Pb}{^{206}Pb}$	±2σ (%)
A293	ZD	40,566	2156	714	0.07	8.953	1.5	0.5445	0.8
A294	ZD	33,035	2732	624	0.06	10.76	2.1	0.4988	2.0
A295	ZD	34,905	3130	737	0.05	10.91	4.8	0.4841	3.7
A296	ZD	74,718	3085	1144	0.06	7.047	2.6	0.6005	2.5
A297	ZD	103,547	4573	1227	0.11	9.921	3.1	0.5130	4.6
A298	ZD	20,847	2981	443	0.06	14.32	1.7	0.3883	2.0
A299	ZD	64,248	2821	773	0.08	8.097	1.9	0.5657	5.0
A300	ZD	5,465	728	183	0.06	8.511	1.6	0.5788	4.0
A301	ZD	15,341	623	468	0.04	2.897	2.0	0.7388	2.8
seq 2									
A411	H4	27,247	145	650	1.76	0.830	4.5	0.8343	1.0
A412		9,201	344	142	0.58	5.171	5.2	0.8032	1.4
A413		11,788	476	192	0.17	5.727	4.1	0.8239	0.9
A414		8,140	351	115	0.16	6.013	5.7	0.8099	1.1
A415		6,624	216	86	0.01	4.581	7.3	0.8178	1.3
A417		9,325	147	145	0.03	2.228	7.8	0.8224	1.0
A418		35,481	169	954	3.89	0.678	2.9	0.8291	1.0
A419		20,135	237	494	1.89	1.660	7.4	0.8203	0.9
A420		25,571	131	869	2.81	0.735	4.8	0.8352	0.7
A421		9,540	330	122	0.52	4.829	6.5	0.8129	0.8
A422		7,881	236	137	2.50	4.205	5.6	0.8183	1.1
A423		15,049	103	409	1.62	0.968	6.7	0.8278	1.3
A424		15,749	126	422	3.92	1.144	6.7	0.8362	0.9
A425		10,392	694	384	0.30	9.302	10.4	0.8128	1.4
A426		14,342	342	259	1.12	3.348	7.0	0.8185	1.6
A427		12,086	75	265	4.52	0.878	5.0	0.8271	1.0
A428		10,305	145	256	2.53	2.002	6.1	0.8317	1.5
A429		7,578	509	101	0.16	9.268	6.2	0.8062	2.0
A430		13,903	147	190	0.32	1.508	6.2	0.8330	1.6
A431		6,663	692	98	0.01	14.090	5.4	0.7936	0.99
A432		5,232	471	80	0.07	12.130	5.3	0.7874	1.3
A433		5,442	733	81	0.35	17.934	4.7	0.7786	0.86
A434		84,409	291	2030	2.03	0.488	2.2	0.8280	0.91
A435		17,755	176	280	0.90	1.418	5.4	0.8380	0.96
A436		32,074	98	2214	7.32	0.433	5.8	0.8279	0.72
A437		15,681	186	695	2.90	1.678	7.5	0.8307	1.0
A438		6,322	736	138	0.88	15.662	2.7	0.7893	1.5
A444		5,129	460	77	0.87	12.246	5.1	0.8017	1.4
A445		2,535	146	54	0.16	7.949	6.2	0.8083	1.4
A447		10,591	394	142	0.02	5.214	5.1	0.8242	1.7
A448		11,030	101	357	3.40	1.287	4.8	0.8271	1.4
A450	H3	12,141	736	138	0.08	13.106	4.1	0.7915	2.4
A451		18,315	460	77	1.89	2.059	7.9	0.8283	0.93
A452		25,108	146	54	0.84	1.966	5.3	0.8432	1.4
A453		31,460	0	0	0.12	1.521	3.4	0.8353	2.4
A454		10,764	394	142	0.08	4.931	4.5	0.8234	1.6
A455		25,746	101	357	0.07	2.372	4.3	0.8395	2.0
A456		25,729	498	203	0.14	2.228	4.1	0.8336	1.5
A457		17,225	1182	201	0.04	4.095	2.6	0.8260	1.2
A458		24,496	268	246	0.16	2.644	4.6	0.8191	0.87
A459		36,070	344	351	0.07	2.352	8.1	0.8355	1.5
A460		40,509	337	387	1.00	1.357	2.8	0.8296	0.88
A461		23,002	379	159	0.06	2.711	3.8	0.8349	1.7
A462		13,414	429	486	5.41	1.038	1.6	0.8328	0.69
A463		48,113	405	592	0.08	2.055	5.4	0.8362	1.3
A464		50,132	503	250	0.07	1.270	4.4	0.8270	1.9
A465		69,182	466	858	0.22	0.905	3.5	0.8324	0.89
A466		16,563	599	673	0.10	13.605	5.5	0.7925	1.1
A467		89,384	391	2140	1.14	0.923	2.9	0.8311	0.89
A468		72,283	441	387	1.06	1.115	3.5	0.8271	0.54

Table 2. (continued)

Spot	Sample ID	$^{207}Pb^{b}$ (c/s)	U^{c} (ppb)	Pb^{c} (ppb)	$\frac{Th}{U}^{c}$	$\frac{^{238}U}{^{206}Pb}$	±2σ (%)	$\frac{^{207}Pb}{^{206}Pb}$	±2σ (%)
A469		27,812	99	5105	1.35	2.016	3.2	0.8202	0.83
A470		16,864	698	765	0.03	11.610	2.9	0.8017	1.3
A471		25,365	454	801	0.88	0.838	4.8	0.8246	1.2
A472		9,554	444	1777	0.06	10.981	3.5	0.8045	1.1
A473		47,793	1680	397	1.30	1.522	5.5	0.8335	2.2
A474		18,856	586	3214	0.21	9.901	3.5	0.8058	1.0
A475		22,813	576	5876	0.69	5.010	2.6	0.8174	1.0
A476		16,460	417	2171	0.36	3.571	3.8	0.8219	2.2
A477		17,035	1489	255	0.08	8.977	3.4	0.8097	2.1
A478		8,174	152	1070	0.27	5.241	4.0	0.8209	1.5
A479		9,159	772	137	0.13	10.185	4.8	0.7962	2.4
A480		8,518	517	788	1.64	4.421	3.5	0.8146	2.6
A481		7,398	1373	1077	0.28	6.901	4.1	0.8212	2.1
A482		44,579	828	911	0.95	1.171	6.0	0.8330	1.5
A483		33,036	437	300	1.03	0.887	2.6	0.8271	0.92
A484		28,352	1119	222	2.80	0.719	2.1	0.8239	0.96
A485		28,614	309	130	0.24	2.190	3.2	0.8214	3.4
A486		26,950	695	119	2.38	1.090	3.7	0.8249	0.69
A487		11,299	274	115	0.36	2.714	3.0	0.8191	1.4
A488		6,053	369	111	0.68	4.246	7.1	0.8215	1.1
A489		25,342	372	640	0.27	1.405	2.1	0.8171	1.2
A490		7,473	211	779	0.24	4.054	5.9	0.8102	1.3
A491		15,925	147	1506	0.24	1.016	3.8	0.8282	1.2
A492		179	453	511	0.38	2.291	7.7	0.8601	5.8
A501	H4-2	19,893	35	500	3.39	0.248	2.3	0.8284	1.2
A502		221,306	453	4422	2.59	0.519	5.2	0.8345	0.55
A504		179,236	1175	3846	2.71	1.337	3.9	0.8303	0.51
A505		43,946	147	996	5.19	0.580	3.5	0.8301	0.85
A506		58,203	78	1215	5.48	0.292	3.6	0.8354	0.90
A508		2,725	18	46	0.93	2.935	3.3	0.8190	1.3
A509		345	7	10	2.19	3.186	6.1	0.8152	3.6
A510		773	103	14	4.83	17.167	5.6	0.7935	1.4
A511		1,731	62	26	5.25	8.285	3.2	0.8041	2.1
A512		886	105	19	6.47	17.156	3.0	0.7909	1.8
A513		10,091	52	262	8.91	0.631	3.0	0.8278	1.5
A514		1,708	48	37	13.43	5.214	7.1	0.8226	3.4
A515		12,079	67	262	7.46	1.084	2.5	0.8301	1.0
A517		9,598	76	155	12.56	3.534	9.4	0.8241	1.7
A518		20,433	94	563	5.92	0.513	4.0	0.8306	1.0
A519		542	57	7	11.63	17.289	7.4	0.7736	2.1
A520		504	15	12	18.32	5.491	6.1	0.8211	2.7
A521		3,119	29	68	18.88	1.437	5.9	0.8215	1.2
A525		408	25	13	20.90	10.390	2.9	0.8070	1.4
A526		2,019	41	37	11.33	7.117	8.7	0.8172	2.8
A527		39,874	186	949	8.87	0.716	2.6	0.8330	1.0
A529		240	31	6	11.02	18.03	3.4	0.7756	4.1
A539		9,487	50	149	5.08	2.046	12.4	0.8245	1.9
A540		46,301	176	1100	6.07	0.687	4.0	0.8368	0.67
A541		12,512	72	221	11.14	1.827	7.3	0.8298	1.2
A542		1,989	9	44	17.82	0.941	2.8	0.8338	1.1
A543		15,925	43	359	16.82	0.466	5.1	0.8333	0.77
A545		11,107	60	232	4.25	1.180	9.9	0.8330	1.4
A546		831	11	19	11.03	2.337	5.8	0.8167	4.8
A547		23,787	65	418	7.34	0.797	9.1	0.8366	0.73
A556		39,969	109	854	7.54	0.600	6.5	0.8259	0.85
A557		221,015	642	5762	4.28	0.356	2.2	0.8347	0.55
A559		44,201	105	743	5.04	1.078	10.0	0.8243	0.71
A560		6,345	42	101	9.03	2.193	7.0	0.8205	1.8
A561		17,223	46	170	16.63	1.039	4.7	0.8234	0.97
A565		434	48	11	17.41	18.05	2.9	0.7837	2.7

Table 2. (continued)

Spot	Sample ID	$^{207}Pb^b$ (c/s)	U^c (ppb)	Pb^c (ppb)	$\frac{Th^c}{U}$	$\frac{^{238}U}{^{206}Pb}$	±2σ (%)	$\frac{^{207}Pb}{^{206}Pb}$	±2σ (%)
A566		5,607	21	144	9.24	0.359	3.4	0.8402	1.5
A567		5,232	50	82	21.85	2.059	2.9	0.8183	1.7
A574		1,814	23	46	14.45	1.864	3.8	0.8333	1.8
A576		4,371	5.1	124	0.18	0.132	3.9	0.8394	2.5
Zechstein Dolomite, Gypsum pit, Tettenborn, Germany									
A05	ZD	16,649	1589	349	0.036	13.09	2.8	0.3944	3.2
A37	ZD	167,051	1834	2160	0.058	2.973	3.6	0.7045	0.74
A71	ZD	18,718	1901	378	0.040	13.34	2.2	0.3801	3.6
A106	ZD	15,030	1611	283	0.040	13.58	2.8	0.3732	5.3
A150	ZD	29,139	1472	501	0.049	8.783	2.5	0.5296	2.5
A242	ZD	21,621	1617	420	0.043	10.93	2.2	0.4605	4.0
A287	ZD	12,540	1620	282	0.046	14.09	1.9	0.3752	2.7
A332	ZD	14,766	1782	313	0.038	13.36	2.5	0.3865	3.4
A377	ZD	15,110	2084	374	0.036	13.53	2.6	0.3835	3.5
A378	ZD	28,864	1867	580	0.047	9.067	2.6	0.5116	1.6
A379	ZD	89,229	1904	1620	0.064	3.897	11.6	0.6607	0.65
A380	ZD	17,954	1907	382	0.046	12.2	1.9	0.4194	1.4
A381	ZD	24,293	1395	477	0.051	8.278	3.1	0.5470	2.3
A382	ZD	13,741	1584	312	0.038	12.41	2.3	0.4132	3.0

[a]Spot size = 235 μm; depth of crater ~15 μm. $^{206}Pb/^{238}U$ error is quadratic additions of within-run precision (2 SE) and external reproducibility (2 SD) of NIST SRM-614 reference; $^{207}Pb/^{206}Pb$ error propagation (^{207}Pb signal dependent) following *Gerdes and Zeh* [2009]; ZD = Zechstein dolomite.
[b]Within-run background-corrected mean ^{207}Pb signal in c/s (counts per second).
[c]U and Pb content and Th/U ratio calculated relative to NIST SRM-614 soda-lime glass.

3.2. U-Pb Dating of Calcite Fibers

U-Pb ages were acquired in situ in six polished thick sections (100–150 μm thick) of calcite fibers from four different samples by laser ablation-inductively coupled plasma-mass spectrometry (LA-ICP-MS) at Goethe University Frankfurt, using a modified method described in *Gerdes and Zeh* [2006, 2009]. A ThermoScientific Element 2 sector field ICP-MS was coupled to a Resolution S-155 (Resonetics) 193 nm ArF excimer laser (CompexPro 102) equipped with a two-volume ablation cell (Laurin Technic). Samples were ablated in a helium atmosphere (0.6 l min^{-1}) and mixed in the ablation funnel with 0.7 l min^{-1} argon and 0.02 l min^{-1} nitrogen. Signal strength at the ICP-MS was tuned for maximum sensitivity while keeping oxide formation (monitored as $^{248}ThO/^{232}Th$) below 1% and Th/U fractionation to 1. Static ablation used a spot size of 235 μm and a fluence of <2 J cm^{-2} at 5 Hz. This yielded for National Institute of Standards and Technology Standard Reference Material-614 (NIST SRM-614) a depth penetration of ~0.5 μm s^{-1} and an average sensitivity of 280,000 c/s μg^{-1} for ^{238}U. The detection limit for ^{206}Pb and ^{238}U was ~0.5 and 0.03 ppb, respectively.

Data were acquired in fully automated mode overnight in sequences of 330 to 598 analyses. Each analysis consist of 20 s background acquisition followed by 20 s of sample ablation and 20 s washout. Prior to analysis each spot was preablated for 3 s to remove surface contamination. Soda-lime glass NIST SRM-614 was used as a reference glass together with two carbonate standards to bracket sample analysis.

Raw data were corrected offline using an in-house MS Excel© spreadsheet program [*Gerdes and Zeh*, 2006, 2009]. Following background correction, outliers (±2σ) were rejected based on the time-resolved $^{207}Pb/^{206}Pb$ and $^{206}Pb/^{238}U$ ratios. The $^{207}Pb/^{206}Pb$ ratio was corrected for mass bias (0.6%) and the $^{206}Pb/^{238}U$ ratio for interelement fractionation (~5%), including drift over the sequence time, using NIST SRM-614. Due to the carbonate matrix, an additional offset factor of 0.921 has been applied, which was determined using WC-1 carbonate reference material dated by TIMS (251 ± 2 Ma; E. T. Rasbury, personal communication, 2014). Repeated analyses ($n = 24$) of a Zechstein dolomite (Gypsum pit, Tettenborn, Germany) used as secondary (in-house) standard yielded a lower intercept age of 257.0 ± 4.7 Ma (mean square weighted deviation (MSWD) 1.3), implying an accuracy and repeatability of the method of ~2%. The analytical results are presented in Table 2. Data were plotted in Tera-Wasserburg diagrams and ages calculated as lower intercepts using Isoplot 3.71 [*Ludwig*, 2009]. All uncertainties are reported at the 2σ level.

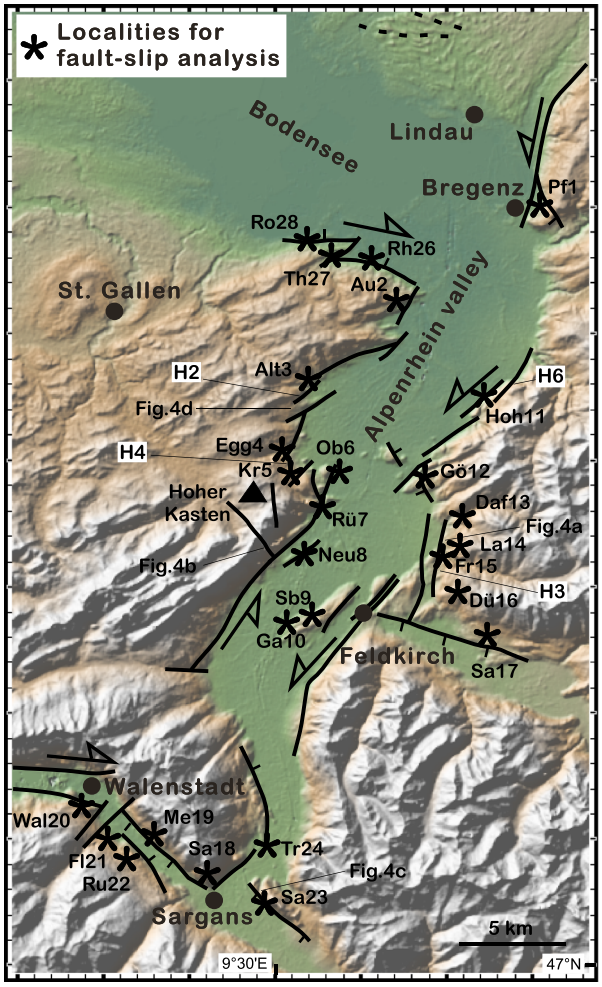

Figure 5. Relief map of eastern Bodensee-Alpenrhein graben system showing main fault traces, locations of photos shown in Figure 4, sample localities for U-Pb dating of fibers (H2, H3, H4, and H6), and stations for fault slip analysis; note that short, sinistral strike-slip fault segments are near vertical; for location of map refer to Figure 2.

4. Fault Slip Data

For addressing the tectonic significance of the Alpenrhein Graben, we mapped faults on either side of the NNE trending valley and also in the NW trending valley between Walenstadt and Sargans, as well as at the southeast end of Bodensee (Figures 3 and 5). Our field work was aided by 1:25,000 geological maps in Switzerland, the 1:200,000 geological map of Vorarlberg in Austria, and 1:50,000 and 1:25,000 maps of the Bodensee region in Germany, as well as maps and cross sections by *Ortner et al.* [2015], *Sala et al.* [2014] and *Pomella et al.* [2015] (Figure 3).

The Alpenrhein Graben is bounded by steep NNE/NE striking planes, which commonly show evidence of tectonic movement such as moderately plunging striations (Figure 4 a). In the Walenstadt-Sargans area, a steep valley bounded by NW striking faults cuts the NNE trending Alpenrhein valley causing a major deflection of the bed of the Alpenrhein river, which flows NW southeast of Sargans (Figures 3 and 5). In addition to the valley-bounding faults a number of faults striking almost perpendicular to the main valley occur (Figures 4b and 4c). Usually, the fault planes show calcite fibers growing from steps on the fault surfaces (Figure 4d); striations and slickensides are also common (Figure 4a). The fibers and slickensides formed by the accretion of fibrous overgrowth. In this case, much if not all of the slip history that occurred on the slip surfaces is preserved in the slickensides. The fiber directions are straight and unidirectional. Thus, we conclude that these kinematic indicators provide a fairly complete record of the slip history [*Ring*, 2008]. Furthermore, the general absence of curved fibers or overlapping fiber directions indicates a relatively simple single-phase history for the studied fault zones in the Alpenrhein Graben.

The faults we mapped in the Alpenrhein Graben do not appear to have been rotated to any significant degree after their formation. The sinistral strike-slip segments are near vertical (Figures 3 and 5) and thus in a typical position for strike-slip faults.

4.1. Alpenrhein Graben

We collected fault slip data from 10 outcrops on the east side (Figure 6) and from eight outcrops on the west side of the valley (Figure 7). Details of the data sets are provided in the figure captions; here only general features will be discussed. The data from the east side are heterogeneous and show site-specific fault sets. The mountain front near Bregenz appears to be controlled by a sinistral strike-slip fault, but fault slip data show NE extension along NNW striking normal faults (Figure 6a). Farther south, the fault sets show an increasing component of sinistral and sinistral-oblique faulting along NE/N striking faults (Figures 6b–6f). A WNW striking graben east of Feldkirch is dominated by normal faults due to NE extension (Figures 6g and 6h). Faulting within an "inselberg" in the Alpenrhein valley just west of Feldkirch shows a heterogeneous and complicated set of faults (Figures 6i and 6j). Overall, shortening directions from the 10 fault sets are

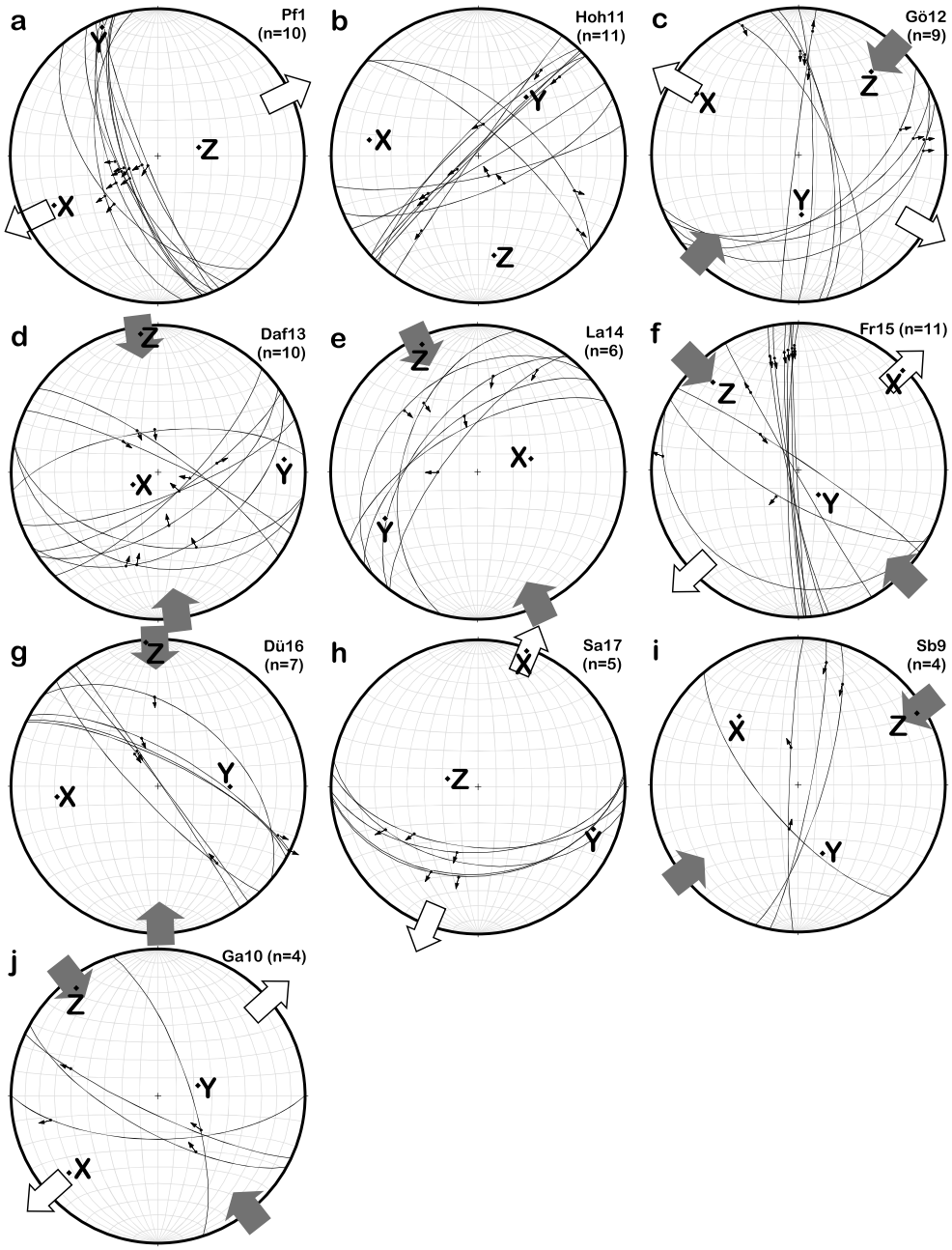

Figure 6. Fault slip data from east side of Alpenrhein Graben; for locations of outcrops refer to Figure 5; diagrams show great circles to fault planes with pole for striation on that fault plane and arrow indicating hanging wall slip direction; principal strain axes ($X > Y > Z$) also shown; hollow arrows are extension direction, grey arrows are shortening direction, and both axes have been projected into horizontal when plunge $<30°$. (a) Outcrop Pf1 dominated by WSW dipping normal faults due to NE extension and subvertical shortening. (b) Station Hoh11 dominated by NE striking sinistral strike-slip faults and two conjugated NW striking dextral faults plus two ENE striking thrusts. (c) Gö12 has NNW striking dextral strike-slip and ENE striking sinistral-oblique normal faults. (d) Outcrop Daf13 shows ENE to ESE striking thrusts and two dextral and one sinistral strike-slip fault. (e) La14 has five NE striking thrusts and one oblique normal fault. (f) Outcrop Fr15 dominated by vertical N-S striking sinistral strike-slip faults. (g) Dü16 shows NW striking dextral strike-slip faults; some have distinct oblique thrust component. (h) Sa17 has E-W striking (dextral-oblique) normal faults. (i) Small data set at station Sb9 with three N-S striking dextral faults and one NW striking dextral-oblique thrust. (j) Complicated data set at Ga10 with WNW striking dextral strike-slip fault, NW striking dextral-oblique thrust, NNW striking sinistral-oblique thrust, and E-W striking dextral-oblique normal fault.

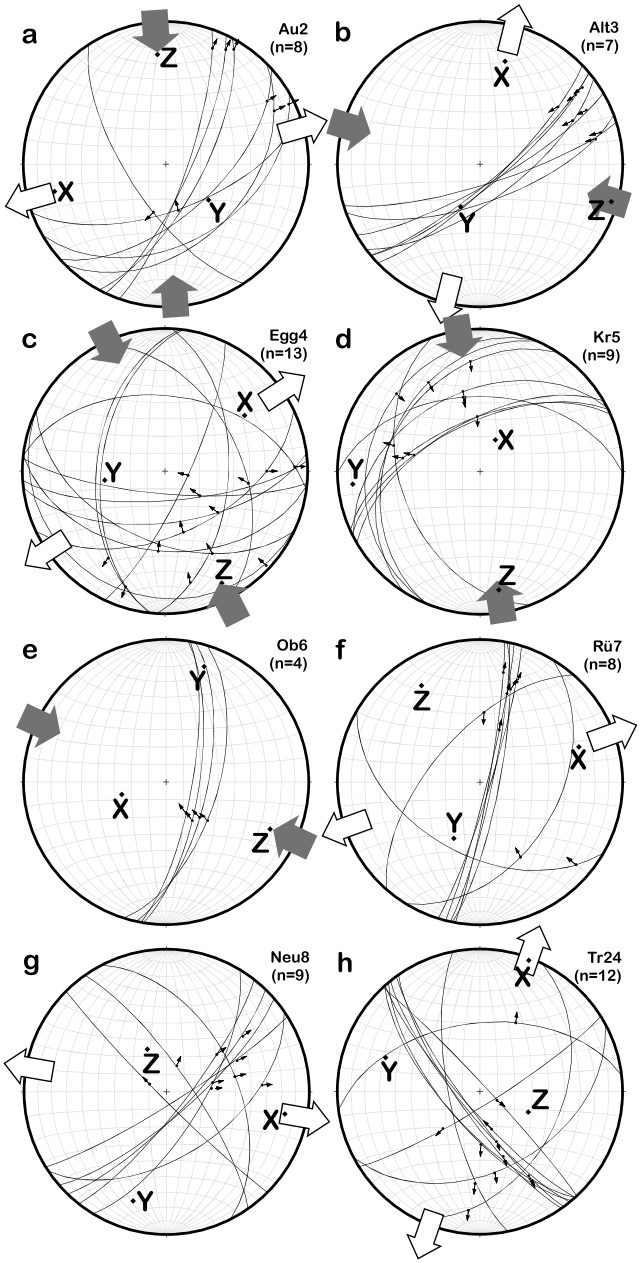

Figure 7. Fault slip data from west side of Alpenrhein Graben; same explanation as for Figure 6; locations of outcrops in Figure 5. (a) Au2 mainly shows NE striking sinistral-oblique normal faults plus one ENE striking thrust and one NW striking normal fault. (b) Simple fault pattern in outcrop Alt3 with seven NE/ENE striking dextral strike-slip faults. (c) Complicated data set at station Egg4 composed of nine roughly E-W striking thrusts and two N-S striking and two ENE striking sinistral-oblique normal faults. (d) Six north to NE striking thrusts and three ENE striking sinistral-oblique normal faults in outcrop Kr5. (e) N-S striking sinistral-oblique thrusts at station Ob6. (g) Rü7 dominated by NNE striking sinistral strike-slip faults plus three oblique thrusts. (h) Neu8 shows NE striking sinistral-oblique normal faults with minor conjugated set of NW striking dextral-oblique normal/strike-slip faults. (i) Tr24 shows dominant set of NW striking dextral strike-slip faults with north to NE striking (sinistral-oblique) normal faults.

preferentially NNW oriented with extension in the NE direction (Figure 6). The data sets show either prolate or oblate strain symmetry (Table 1).

The fault pattern on the west side of the Alpenrhein valley shows a similar heterogeneous data set (Figure 7). A recurring pattern in most outcrops are N/NE striking sinistral faults with pure strike-slip and sinistral-oblique kinematics (Figure 7). These sets appear to be dominant in outcrops Au2, Kr5, Ob6, Rü7, and Neu8, whereas outcrop Alt3 is characterized by NE and Tr24 by NW striking dextral strike-slip faults. As on the east side of the valley, the outcrops on the west side show a NW trending shortening and a NE oriented extension direction. Again, the data record either prolate or oblate strain symmetry.

The data from the Alpenrhein valley are compatible with the fault pattern shown in Figures 3 and 5. There is a dominance of sinistral strike-slip faulting along NNE/NE striking faults. The strike length of these faults is of the order of 5–15 km. Local, smaller scale normal, and reverse faults occur as well.

4.2. Walenstadt-Sargans Valley

The Alpenrhein valley is markedly deflected near Sargans where the flow direction of the Alpenrhein river swings by about 90° from NW to NE. We collected fault slip data from six outcrops along the NW striking valley between Sargans and Walenstadt (Figures 5 and 8). The data from all outcrops but Wal20 (Figure 8a) are dominated by NW striking normal faults (Figures 8b–8f). The normal faults are either NE or SW dipping; in outcrop Ru22 a conjugated set of normal faults occurs. Station Wal20 shows a conjugated set of NE striking sinistral and E-W striking dextral strike-slip faults.

The data sets show NE extension indicating that this valley segment was shaped by NW striking normal faults resulting from NE extension. The data show preferentially oblate strain symmetry. The kinematics of the Sargans-Walenstadt Graben is similar to the WNW striking graben east of Feldkirch (Figures 3 and 5).

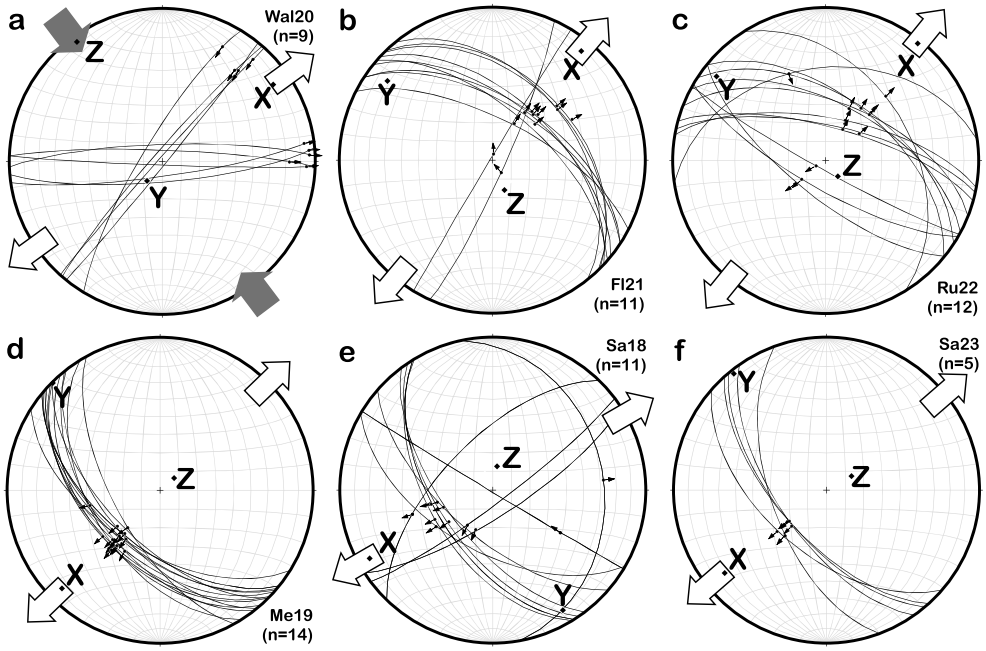

Figure 8. Fault slip data from Sargans-Walenstadt area; same explanation as for Figure 6; for locations of outcrops see Figure 5. (a) Outcrop Wal20 shows conjugated set of NE striking sinistral and E-W striking dextral strike-slip faults. (b) NW striking normal faults, one NE striking thrust, and vertical dextral-oblique normal fault at station Fl21. (c) Conjugate set of NW striking normal faults dominates outcrop Ru22. (d) Simple pattern of NW striking normal faults at outcrop Me19. (e) Outcrop Sa18 also dominated by NW striking normal faults plus NE striking oblique normal faults. (f) Simple set of NW striking normal faults at station Sa23.

Southeast/south of Sargans faulting is much less prominent and becomes diffuse. There are no obvious fault surfaces in the landscape, and small-scale normal and strike-slip faulting appears to be resolved along minor fault surfaces. South of Landquart (Figure 2), even those minor fault surfaces become rare.

4.3. Bodensee

There are hardly any outcrops at the southeast end of Bodensee. We collected fault slip data in Molasse deposits east of St. Gallen (Figure 5). The stations here are dominated by a set of conjugated E-W to ESE striking dextral-oblique normal faults (Figures 9a and 9b). Outcrop Th27 shows a more complex fault pattern with sinistral-oblique thrusts, thrusts, and sinistral-oblique normal faults. The data sets from the eastern end of the

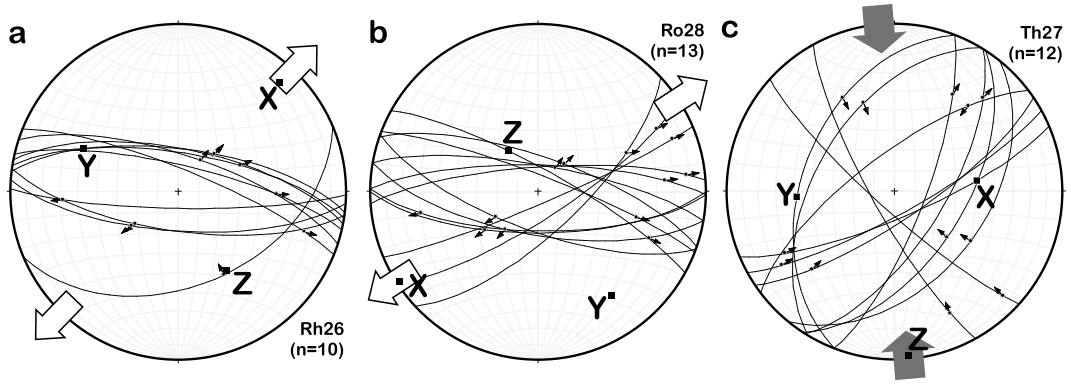

Figure 9. Fault slip data from eastern end of Bodensee; for explanation see Figure 6; for locations see Figure 5. (a) Outcrop Rh26 dominated by E-W to WNW striking normal and dextral-oblique normal faults plus one NE striking thrust. (b) Ro28 has similar faults as Rh26 with pattern of conjugated E-W striking dextral-oblique normal faults and NE striking sinistral strike-slip faults. (c) Station Th27 showing complex fault pattern with NE striking sinistral-oblique thrusts, thrusts, and oblique normal faults plus two conjugated NW striking dextral strike-slip faults.

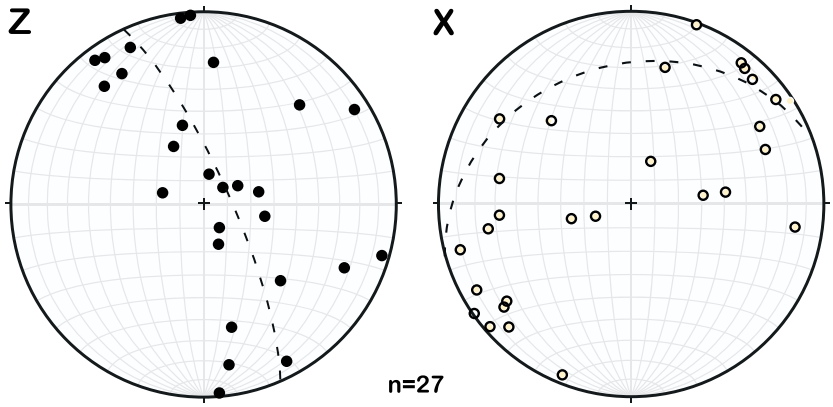

Figure 10. Lower hemisphere equal-area plots of shortening (*Z*) and extension (*X*) directions derived from fault slip analyses (Table 1); *Z* and *X* axes define great-circle distributions (dashed circle) reflecting deformation partitioning into strike-slip, normal, and thrust components.

Bodensee Graben basically resulted from NE extension with a subordinate component of NNW shortening. We have not enough data to infer much about the strain symmetry, but note that both prolate and oblate patterns are recorded.

4.4. Tear Faults in Helvetics

In part, the faults that bound the Alpenrhein Graben are associated with NW striking tear faults in the Helvetic Nappes. The NW/N striking tear faults show either sinistral or dextral kinematics and are associated with lateral changes in the rate of thrust sheet propagation due to differential shortening of the nappe stack [*Funk et al*., 2000]. We studied these transfer faults in the area south of Hoher Kasten (Figures 3 and 5). The fault planes are striking NW to north and are decorated with moderately plunging striations (~10–30°). In some places a second set of striations occurs, and these are distinctly steeper (~35–60°) than the moderately plunging ones. On NW striking faults, the secondary striations plunge at 50–60° and indicate normal displacements, whereas on the north striking faults the striations plunge at 35–50° and relative motion is oblique. Crosscutting relations are sometimes straightforward, and the steep secondary striations overprint the shallow ones. However, in most places this distinction cannot be made and overprinting relations are mutual.

4.5. Kinematic Regime

In Figure 10 we plotted the shortening (*Z*) and extension (*X*) axes derived from fault slip analysis. The shortening axes depict a fairly well developed great-circle distribution with a strike/dip of 336/32 (right-hand rule). The extension axes show more scatter but still define a weak great circle (strike/dip = 252/32). The great-circle arrangement of the principal axes reflects the interplay of strike-slip, normal, and thrust faulting.

According to *Dewey et al*. [1998] transtension can be defined as strike-slip deformation that deviates from simple shear because of a component of extension orthogonal to the deformation zone. In transtension zones instantaneous strain axes and finite strain axes are oblique to one another (cf. Figure 10) leading to complex three-dimensional, noncoaxial strains. One consequence of this is that structures differing significantly in orientation may form simultaneously, especially in the shallower crust where brittle deformation is commonly characterized by complex domains of rotating crustal blocks. Our fault slip data record, at least in part, such heterogeneity. In the simple, constant-volume, vertical stretch model of *Sanderson and Marchini* [1984] transtension zones should generate constrictional strain types. We note that the transtensional zones in the Alpenrhein valley record a mix of prolate and oblate strain symmetry but that the normal fault-dominated graben between Sargans and Walenstadt shows a preference for oblate strain symmetry. Oblate strains in transtension zones can occur depending on the obliquity of the simple shear component and the nature of any kinematic partitioning within the deformation zone [*Dewey et al*., 1998]. Formation of the Alpenrhein Graben was concurrent with NW directed nappe emplacement in the area. Therefore, kinematic partitioning in the Alpenrhein Graben into faults recording strike-slip, normal, and thrust kinematics took place. Given the overall graben structure, the partitioning of dominantly sinistral faulting in the Alpenrhein Graben and normal

faulting in the segments between Sargans-Walenstadt and east of Feldkirch, and the varying directions of the principal strain axes, we infer a transtensional origin of the Alpenrhein Graben.

5. Dating of Calcite Fibers

We have shown that the faults forming the Alpenrhein Graben are decorated with simple, single-phase calcite fibers and striations (Figure 4). Tear faults in the Helvetic Nappes show, in part, striations with complex overprinting relations suggesting that tear faulting and faulting in the Alpenrhein Graben overlapped in time. This observation implies that the faults that structured the Alpenrhein Graben formed during nappe emplacement in the Helvetic Nappes between 35–30 Ma and 25–20 Ma. We made an attempt to verify and substantiate this conclusion by using a novel approach to date calcite fibers associated with faults of the Alpenrhein Graben by the U-Pb method.

In situ U-Pb isotope analyses of calcite fibers from four different samples yielded lower intercept ages of 24.0 ± 6.3 (H2), 21.8 ± 3.4 (H3), 22.3 ± 4.6 (H6), 24.1 ± 3.2 and 25.3 ± 5.6 Ma (H4), and 22.5 ± 3.2 (H4-2) (Figure 11). The two results for H4 were obtained from the same thick section of sample H4 analyzed on two different days. This procedure was done for checking whether the method yields meaningful and reproducible results. For the same reasons we cut another thick section from sample H4 and also analyzed it (H4-2).

All ages suffer from relatively large uncertainties, which are related to the very low concentration of U ($<$1 ppm) and radiogenic Pb, and the limited spread in $^{238}U/^{206}Pb$ ratios. However, the ages are internally consistent and are statistically sound (Figure 11 and Table 2). Given 2σ errors, our ages range between 31 and 18 Ma and thus overlap with thrusting in the Helvetic Nappes. This age span probably reflects a period of ~10 Myr over which the Alpenrhein Graben slowly formed.

The weighted average age of both H4 analyses is 24.4 ± 2.7 Ma. If H4-2 was included, it would be 23.6 ± 2.2 Ma (MSWD = 0.47). This demonstrates that uncertainties can be lowered by pooling results of repeated analyses. Using all six ages, the weighted average U-Pb age is 23.1 ± 1.6 Ma (MSWD = 0.39).

6. Earthquake Data

The U-Pb ages of the calcite fibers show that the Alpenrhein Graben started to form in the late Oligocene and early Miocene contemporaneously with NW directed nappe emplacement in the Helvetics. The kinematics of the Alpenrhein Graben is due to NE extension and NW directed shortening. Here we compare Oligocene/Miocene graben development with earthquake data from northeast Switzerland, south Germany, and east Austria (http://www.seismo.ethz.ch) (Figure 2).

The earthquake data from the Alpenrhein Graben (column on right and bottom of Figure 2, and Buchs, 2000, Walenstadt, 2009, and Oberriet, 2001, in the left column) are all basically strike-slip solutions resulting from NW shortening and NE extension. Only one of the Bad Ragaz, 2000, earthquakes shows kinematics that are 90° different (Figure 2, bottom column). The Buchs, 2000, Feldkirch, 2010, and Vaduz, 2009, earthquakes resulted from almost pure NW shortening (thrust faulting) or NE extension (normal faulting).

The earthquake data from the Bonndorf-Bodensee graben system are similar to the ones from the Alpenrhein valley (Figure 2). The same is true for a few earthquakes from the Helvetics east of the Alpenrhein (Wildhaus, 2009, Neslau, 2003, and Kirchberg, 1996; Figure 2).

Overall, the earthquake data provide similar kinematics as those derived from the fault slip data of exhumed fault zones in the Alpenrhein valley and show that this deformation regime is not confined to the Alpenrhein Graben. The earthquake data also record the partitioning of deformation into predominantly strike-slip faulting but also normal and thrust faulting. This demonstrates that the kinematics and nature of faulting did not change since the onset of transtensional faulting in the Alpenrhein valley and nappe emplacement in the Helvetics in the Oligocene.

7. Discussion

7.1. Kinematics and Timing

The Alpenrhein valley represents a transtensional graben structure at the northern front of the Central Alps. The graben is characterized by relatively short overstepping segments of NNE striking sinistral strike-slip and

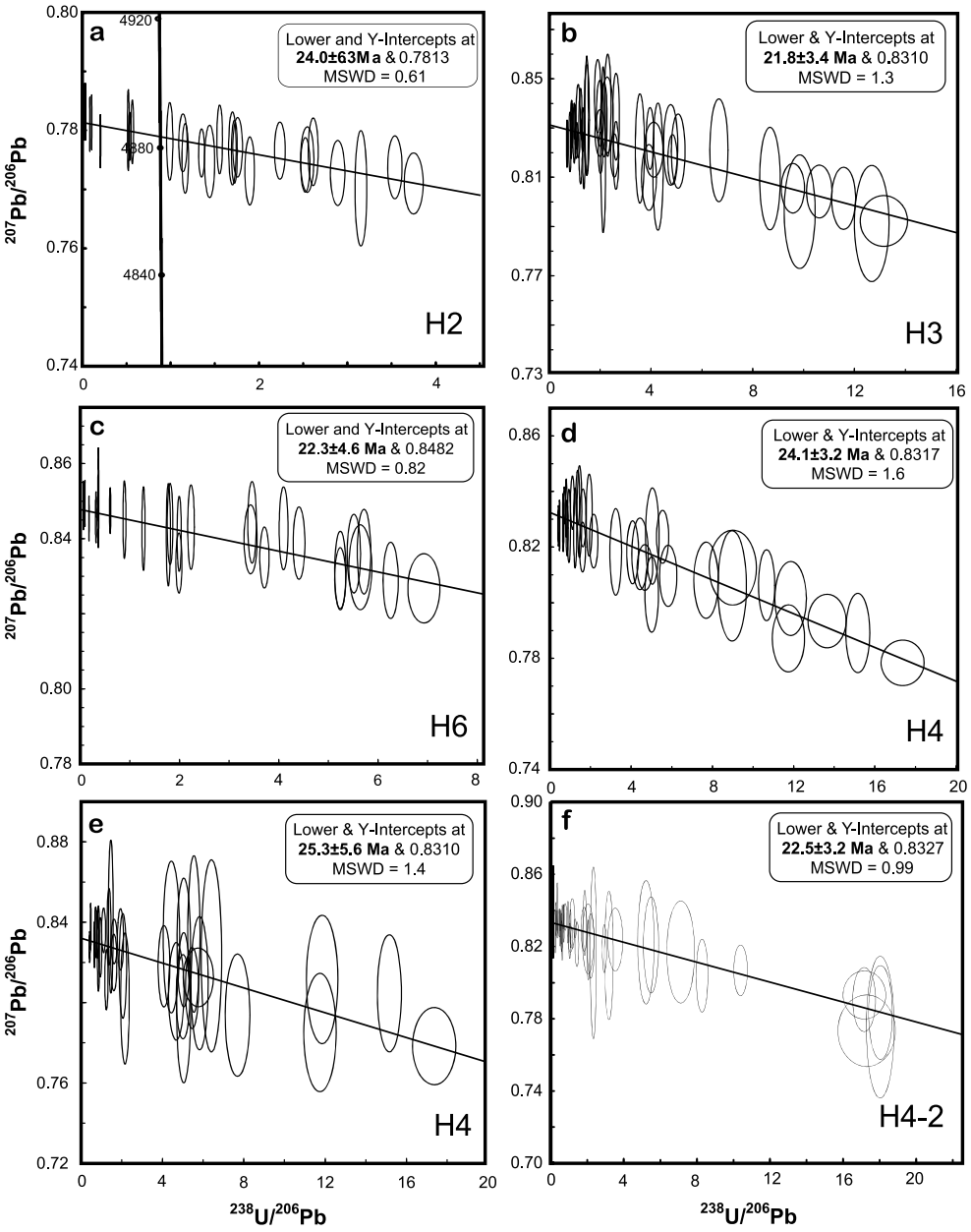

Figure 11. Tera-Wasserburg diagrams of U-Pb isotope data of calcite fibers from four samples; for sample localities see Figure 5. Lower intercept ages correspond to time of fiber crystallization; (d and e) same thick section of sample H4 analyzed on two different days yielding same age within errors; (f) H4-2 also from sample H4 but different thick section.

oblique normal faults. The Sargans-Walenstadt valley is a noticeable cross graben made up by NW striking normal faults. Farther south, the Alpenrhein Graben appears to die out giving the structure an overall V-shaped geometry.

Graben development is closely associated with NW directed thrusting in the Helvetics as suggested by, in part, mutual crosscutting relations of nappe emplacement and graben-related striations. N-S trending vertical strike-slip faults (e.g., Sax-Schwende Fault in Figure 3) accommodating left-lateral motion concomitant with nappe imbrication [*Funk et al.*, 2000; *Sala et al.*, 2014] is in line with our reasoning that left-lateral strike-slip faulting and thrusting were coeval and suggests that the wrench corridor was not confined to the Alpenrhein valley. Direct U-Pb dating of brittle deformation provided internally consistent ages ranging from 25.3 ± 5.6 Ma to 21.8 ± 3.4 Ma for growth of calcite fibers, which agree well with the structural observations. Interestingly, the kinematics derived from earthquake data are similar to the fault slip kinematics

derived from exhumed fault surfaces. Therefore, it appears that the kinematics in the greater Alpenrhein valley area did not change since the Oligocene onset of graben development until the Recent. However, the thrust zone between the Säntis Nappe and the imbricated Molasse is not significantly displaced by sinistral transtensional faulting (see also *Funk et al*. [2000]) and this contact is post middle Miocene in age (<12 Ma) [*Funk et al*., 2000]. Our interpretation is that the main activity of the Alpenrhein Graben was concurrent with nappe emplacement in the Helvetics and then slowed down considerably. Whether or not there was a distinct lull in faulting activity cannot be answered with our data, but NW shortening and NE extension is currently active as indicated by the earthquake data. The regional tectonic perspective shows that NW directed shortening and nappe translation until ~12 Ma was by far more important than NE directed extension, the latter of which was locally accommodated, with the Alpenrhein Graben being the main structure. This also shows that regionally the tectonic regime was dominated by shortening and that transtensional graben development was a minor event superimposed on nappe emplacement.

Oligocene to early Miocene sinistral transtension across the Alpenrhein Graben helps explaining the rather drastic change in the outcrop pattern of the Alpine nappe stack (Figure 3). Given the prominent outcrops of Pennine and Austroalpine nappes east of the Alpenrhein valley, the downdrop of the east side appears to be of the order of several kilometers.

The WNW striking Bonndorf-Bodensee graben system resulted from dextral transtension and together with the Alpenrhein Graben constitutes a conjugated graben system within the northern Central Alps and its adjacent foreland. A minimum age of 18 Ma for the formation of the Bonndorf-Bodensee graben system broadly fits with the age of formation of the Alpenrhein Graben. Because the extrusion of the Hegau volcanics from ~16–8 Ma were controlled by faults, graben development in the Bonndorf-Bodensee graben system had significant activity in the middle/late Miocene, while tectonic activity in the Alpenrhein Graben already largely ceased before ~12 Ma. This temporal relationship seems best interpreted by propagation of graben tectonics from south to north.

7.2. Tectonic Model

Our maximum age for the onset of faulting in the Alpenrhein Graben is 31 Ma. Important is that Oligocene to early Miocene graben development in the frontal parts of the evolving Alpine orogen can be temporally linked to graben formation in the foreland. Therefore, extensional deformation can hardly be explained by gravitational (thermal) collapse and it is likely that extension has been triggered by another mechanism. In this section we speculate on large-scale forces that may have driven tangential stretching in the Central Alps. Our model is sketched in Figure 12 and largely based on models of subduction zone rollback in the west Mediterranean as proposed by *Lonergan and White* [1997], *Rosenbaum et al*. [2002], *Faccenna et al*. [2004], and *van Hinsbergen et al*. [2014].

Tangential stretching in the Central Alps was under way by ~35–32 Ma [*Challandes et al*., 2003]. Movement in the Simplon ductile shear zone probably started at 32 Ma, certainly before 30 Ma [*Steck*, 2008]. Top-to-the-E/ENE brittle-ductile extension in the eastern Central Alps began before 32–30 Ma [*Ring*, 1994; *Nievergelt et al*., 1996], and E-W extension in the Eastern Alps commenced at ~30 Ma [*Glodny et al*., 2008]. Tangential stretching in the Central and also the Eastern Alps is thus coeval with the main phase of E-W to NE-SW extension across the ECRIS graben in the foreland of the Central and Western Alps and the Alpenrhein Graben at ~34–30 Ma. This main phase of extension in the Alps was termed "Oligocene Lull" by *Laubscher* [1983]. However, it needs to be stressed that the onset of E-W extension in the Alps was coeval with N/NW directed nappe stacking [*Hunziker et al*., 1986; *Schmid et al*., 2004; *Glodny et al*., 2008]. *Rosenbaum et al*. [2002] summarized that extension in the west Mediterranean basins also commenced by 32–30 Ma.

Our conceptual tectonic model starts with a largely noncurved Eocene Alpine orogen ranging from the Pyrenees via the Alps into the Carpathians (Alcapa in Figure 12a). The convergence rates between Africa and Europe increased at about this time [*Dewey et al*., 1989]. Subduction of oceanic and continental lithosphere in the Alps is to the southeast, whereas it is to the northwest in the west Mediterranean orogens [*Rosenbaum et al*., 2002]. Differential shortening between these two orogenic domains may have triggered initial sinistral movement in nascent ECRIS. Such an interpretation would broadly be in line with orogenic foreland splitting as proposed by *Sengör* [1976].

In the early Oligocene, the Alps farther propagated north and subduction zone rollback commenced in the west Mediterranean, broadly coeval with tangential stretching in the Central and Eastern Alps (Figure 12b).

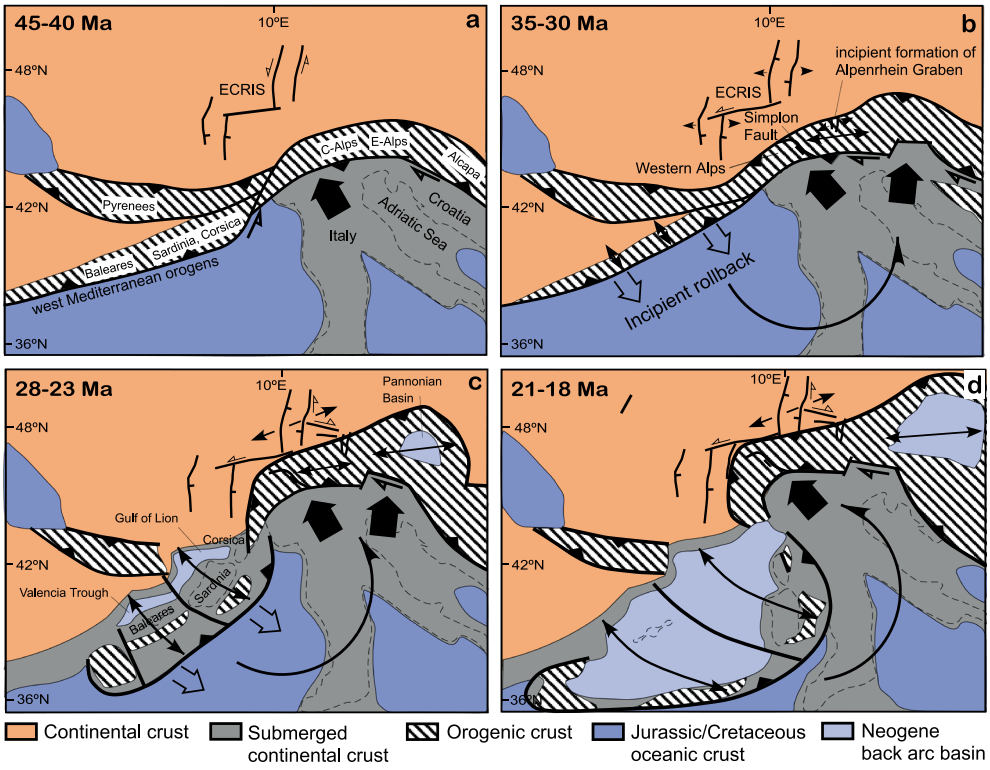

Figure 12. Simplified sketches illustrating tectonic model linking tangential stretching in Central Alps and its foreland to rollback of west Mediterranean subduction zone, rotation of Adria, and development of Western Alps arc; approximate outlines of Italy/Croatia and Corsica, Sardinia, and Balearic islands shown for reference. (a) Eocene situation characterized by NW directed thrusting and high-pressure metamorphism in Central Alps; rollback had not yet commenced in west Mediterranean; incipient strike-slip faulting in Oberrhein and Bresse-Rhône Graben north of transition zone between NW directed thrusting in Alps and SW directed thrusting in west Mediterranean orogens; differential motion associated with transition zone may have controlled continental foreland splitting [cf. *Sengör*, 1976] (note that Adria is upper plate only in Alps and lower plate farther west and east; heavy lithosphere of Adria controls subduction zone retreat in Mediterranean [*Ring et al*., 2010]). (b) NW dipping subduction zone in west Mediterranean started to roll back in early Oligocene; submerged crust of Adria rotated counterclockwise with respect to Europe causing NW and north directed shortening at its northern margin; Western Alps accommodated west Mediterranean rollback and rotation of Adria by counterclockwise rotation. Extension in Calabria, Sardinia, Corsica, Ligurian Sea, and Gulf of Lion commenced by 32–30 Ma [*Brunet et al*., 2000; *Rosseti et al*., 2001]. In Alps, Simplon Fault started to form as strike-slip fault and Central Alps underwent modest E-W extension; European foreland undergoes E-W extension along ECRIS; Alpenrhein Graben may have started to form by this time; how much Western Alps arc was curved before west Mediterranean rollback commenced is hardly known. (c) Late Oligocene; progressing west Mediterranean subduction zone rollback causing opening of Gulf of Lion and Valencia Trough back-arc basins; Adria and Western Alps continued to rotate counterclockwise; further movement on Simplon Fault, E-W stretching in Central Alps, Alpenrhein Graben underwent sinistral transtension; Pannonian Basin opened east of Alps as response of eastward rollback of subduction zone in east. (d) Early Miocene; advanced stage of rollback in west Mediterranean and continued rotation of Adria; Western Alps arc largely reached current shape; Provençal Basin became oceanic (21.5 Ma [*Carminati et al*., 1998]); Limagne and Bresse-Rhône Graben system became inactive by 20–18 Ma [*Michon and Merle*, 2001], Oberrhein Graben remains active until present day. Reconstructions largely based on *Rosenbaum et al*. [2002].

Incipient rollback of the west Mediterranean subduction zone around a rotation pole in present northwest Italy started to open the Gulf of Lion and the Ligurian Sea and caused horizontal extension in Corsica and Sardinia [*Brunet et al*., 2000; *Rosseti et al*., 2001; *Zarki-Jakni et al*., 2004; *Faccenna et al*., 2004]. Rotational rollback and the opening of the west Mediterranean basins were associated with counterclockwise rotation of Adria, which in turn increased the curvature of the Western Alps arc [*Maffione et al*., 2008]. We argue that the increasing curvature caused the Simplon Fault to form in the hinge of the rotating arc. In other words, dextral extension in the hinge zone is geometrically accommodating the rotation of the Western Alps. The increasing curvature is mainly taken up by the Simplon Fault but is also causing limited E-W stretching in the Central Alps, which is resolved in the eastern Central Alps by normal faulting across the Turba mylonite zone and reactivation of former nappe contacts in the Pennine nappes of eastern

Switzerland [*Ring*, 1994; *Nievergelt et al*., 1996]. *Ring* [1992] showed that the amount of E-W extension was modest. The Tauern Window in the Eastern Alps also started to extend by 30 Ma [*Glodny et al*., 2008]. By far most of the large-scale E-W extension east of the Tauern Window, and in part also within the Tauern Window, was due to lateral eastward extrusion caused by rollback of a subduction zone in the Carpathians and the opening of the Pannonian Basin in the Miocene [*Ratschbacher et al*., 1991]. However, there is limited E-W extension prior to Miocene lateral extrusion and this early extension might be due to far-field space problems resulting from the increased curvature of the Western Alps arc.

The increasing curvature of the Western Alps arc was accompanied by continuing NW directed nappe emplacement in the Central Alps, and the Helvetics had its main phase of movement at 35–30 Ma [*Hunziker et al*., 1986]. Because there is an intimate relationship between nappe emplacement-related tear faults and the Alpenrhein faults, it is conceivable that the Alpenrhein Graben started to form at this time. This would be in line with our ages of fault-controlled fiber growth, but we admit that 2σ errors are rather large.

During the initial stage of rollback of the west Mediterranean subduction zone in the early Oligocene, ECRIS had its main rifting phase characterized by vertical shortening and E-W extension [*Lacombe et al*., 1993; *Merle et al*., 1998; *Merle and Michon*, 2001; *Michon and Merle*, 2001; *Schumacher*, 2002]. This main rifting phase led to marine conditions in the Oberrhein Graben and Molasse basin [*Sissingh*, 2001] due to a combination of extension/subsidence and sea level rise [*Miller et al*., 2011].

In the next stage of our model (Figure 12c), progressive rollback in the west Mediterranean opened the Valencia Trough and the Provençal Basin [*Faccenna et al*., 2004; *Maffione et al*., 2008]. In the Alps, the curvature of the arc further increased, and E-W and NE-SW extension continued. At the end of this phase, major E-W extension in the Eastern Alps commenced (see above). The main extension across the ECRIS graben system ceased, and the graben bounding faults underwent sinistral strike-slip faulting again. *Dezes et al*. [2004] related renewed strike-slip faulting in the Oberrhein Graben to the cessation of compression in the Pyrenees. We believe that the counterclockwise rotation of Adria caused increasing shortening in the Alps and may have contributed to intensified NW directed shortening at the front of the Alps aiding rotation of the main compressive stress into a horizontal position.

In the final step (Figure 12d), the Provençal Basin became oceanic by 21.5 Ma [*Carminati et al*., 1998] and takes up most of the extension in the west Mediterranean. Therefore, the Limagne-Bresse-Rhône graben system became inactive by 20–18 Ma [*Michon and Merle*, 2001]. The graben that are not directly affected by this transfer in extension deformation, i.e., the Alpenrhein, the Bonndorf-Bodensee, and the Oberrhein Graben, remained active. At ~19–18 Ma, Africa-Europe convergence slowed down considerably [*Dewey et al*., 1989]. This is when the Schwarzwald and Vosges mountains started to uplift and volcanism in the Hegau commenced, suggesting a causal connection between these processes. The slowing down of Africa-Europe convergence eventually slowed down the rate of nappe advance in the Helvetics over the Molasse, and this tectonic contact is hardly affected by faulting in the Alpenrhein/Bodensee area.

According to our model, the strongly curved shape of the Western Alps was, at least in part, caused by rollback of the west Mediterranean trench [see *Maffione et al*., 2008]. We interpret the V-shaped Alpenrhein Graben as an effect of "outer-arc stretching" superimposed on NW directed nappe emplacement. Furthermore, we speculate that limited Oligocene tangential stretching in the Central and probably also the Eastern Alps was also controlled by the rotation of the Western Alps arc.

7.3. Implications for Alpine Tectonics

Our attempt linking tangential stretching in the Central and Eastern Alps with subduction zone rollback and associated increased counterclockwise rotation of Adria has implication for large-scale models of nappe stacking and high-pressure metamorphism in the Alps [*Schmid et al*., 2004]. These models are largely cylindrical and use crosscutting relations of the Bergell intrusion (32–30 Ma) in the Central Alps (Figure 1) to argue that nappe emplacement and associated high-pressure metamorphism in the internal parts of the Alps was completed by 32–30 Ma. Pre-Bergell high-pressure metamorphism is well established in the Central and Western Alps with ages of ~70–35 Ma for the peak of high-pressure metamorphism [*Reddy et al*., 1999; *Gebauer*, 1999; *Angiboust et al*., 2014]. However, there is incontrovertible evidence that high-pressure metamorphism in the Tauern Window of the Eastern Alps occurred later at 32–30 Ma [*Glodny et al*., 2005, 2008; *Gleissner et al*., 2007; *Smye et al*., 2011].

In Figure 12a, Eocene northwestward movement of Adria results in almost orthogonal convergence in the Central Alps, whereas convergence farther east is distinctly more oblique. Oligocene trench rollback in the west Mediterranean caused not only increased counterclockwise rotation of Adria but also pushed its northeastern edge northward (Figure 12b) This in turn causes more frontal convergence in the Eastern Alps and may explain why high-pressure metamorphism in Eastern Alps occurs later than in the Central and Western Alps. *Glodny et al*. [2005] and *Smye et al*. [2011] showed that underthrusting in the Eastern Alps was rapid at ~34–32 Ma facilitating high-pressure metamorphism very soon after the onset of convergence. Convergence-related high-pressure metamorphism in the Tauern Window of the Eastern Alps overlapped in time with the formation of the Western Alps arc and tangential stretching in the Central and Eastern Alps. The relatively late high-pressure metamorphism in the Tauern Window indicates that crosscutting relations of the Bergell intrusion at 32–30 Ma cannot be used for inferring nappe emplacement in the entire Alps.

8. Concluding Remarks

We have provided evidence for sinistral transtensional faulting in the Alpenrhein Graben in the Oligocene and early Miocene. Sinistral transtension along the NNE trending Alpenrhein valley is conjugated with dextral transtension along the WNW trending Bonndorf-Bodensee graben system. The formation of the Alpenrhein Graben can broadly be linked to the main phase of extension in the Oberrhein, Limagne, and Bresse-Rhône graben systems.

We discussed a model explaining the formation of the V-shaped Alpenrhein Graben by outer-arc stretching resulting from the increasing curvature of the Western Alps arc. We also proposed that the increased curvature of the Alpine arc had, in part, been shaped by rollback of the west Mediterranean trench. Furthermore, we speculated that the Oligocene E-W stretching history in the Central and Eastern Alps is also related to incipient rollback in the west Mediterranean. Tangential stretching in the Central Alps included the formation of Simplon Fault and pre-Bergell extension in the eastern Central Alps.

Acknowledgments
U.R. was funded by Stockholm University. We thank Meinert Rahn, Tobias Ibele, and Daniel Egli for discussions. A careful review by Kamil Ustaszewski and comments by the Editors helped to improve our paper. Readers can access the data reported in this manuscript at http://people.geo.su.se/uwe/.

References

Ahorner, L. (1975), Present-day stress field and seismotectonic block movements along major fault zones in central Europe, *Tectonophysics*, *29*, 233–249.

Allmendinger, R. W., N. C. Cardozo, and D. Fisher (2012), *Structural Geology Algorithms: Vectors & Tensors*, pp. 289, Cambridge Univ. Press, Cambridge, U. K.

Angiboust, S., J. Glodny, O. Oncken, and C. Chopin (2014), In search of transient subduction interfaces in the Dent Blanche–Sesia Tectonic System (W-Alps), *Lithos*, *205*, 298–321.

Argand, E. (1924), La Tectonique de l'Asie, *Compte-rendu du 13e congrès*, *Géol. Int.*, 171–372.

Bellaiche, G., F. Irr, and M. Labarbarie (1976), Decouverte de sediments marins fini oligocene-aquitanien au large du Massif des Maures (Canyon des Stoechades), *C. R. Acad. Sci. Paris*, *283*, 319–322.

Bergerat, F. (1987), Stress fields in the European platform at the time of Africa-Eurasia collision, *Tectonics*, *6*, 99–132, doi:10.1029/TC006i002p00099.

Bertle, H. (1970), Kurze Mitteilung über ein NNE-SSW-streichendes Lineament zwischen Lechtal und Klosters, *Verh. Geol. B. Anst.*, *3*, 469–490.

Brunet, C., P. Monié, L. Jolivet, and J. P. Cadet (2000), Migration of compression and extension in the Tyrrhenian Sea, insight from $^{40}Ar/^{39}Ar$ ages on micas along a transect from Corsica and Tuscany, *Tectonophysics*, *321*, 127–155.

Calais, E., J. M. Nocquet, F. Jouanne, and M. Tardy (2002), Current strain regime in the Western Alps from continuous Global Positioning System measurements, 1996–2001, *Geology*, *30*, 651–654.

Carey, S. W. (1958), A tectonic approach to continental drift, in *Continental Drift: A Symposium*, edited by S. W. Carey, pp. 177–355, Geology Department, Univ. of Tasmania, Hobart.

Carminati, E., M. J. R. Wortel, W. Spakman, and R. Sabadini (1998), The role of slab detachment processes in the opening of the western-central Mediterranean basins: Some geological and geophysical evidence, *Earth Planet. Sci. Lett.*, *160*, 651–665.

Challandes, N., D. Marquer, and I. M. Villa (2003), Dating the evolution of C–S microstructures: A combined $^{40}Ar/^{39}Ar$ step-heating and UV laserprobe analysis of the Alpine Roffna shear zone, *Chem. Geol.*, *197*, 3–19.

Champagnac, J. D., C. Sue, B. Delacou, P. Fricart, C. Allanic, and M. Burkhardt (2006), Miocene lateral extrusion in the inner Western Alps revealed by dynamic fault analysis, *Tectonics*, *25*, TC3014, doi:10.1029/2004TC001779.

Channell, J. E. T., B. D'Argenio, and F. Horvath (1979), Adria, the African promontory, in Mesozoic Mediterranean palaeogeography, *Earth Sci. Rev.*, *15*, 213–292.

Cherchi, A., and L. Montadert (1982), Oligo-Miocene rift of Sardinia and the early history of the western Mediterranean basin, *Nature*, *298*, 736–739.

Ciancaleoni, L., and D. Marquer (2008), Late Oligocene to early Miocene lateral extrusion at the eastern border of the Lepontine dome of the central Alps (Bergell and Insubric areas, eastern central Alps), *Tectonics*, *27*, TC4008, doi:10.1029/2007TC002196.

Collombet, M., J. C. Chauvin, A. Bouillin, and J. P. Gratier (2002), Counterclockwise rotation of the Western Alps since the Oligocene: New insights from paleomagnetic data, *Tectonics*, *21*(4), 1032, doi:10.1029/2001TC901016.

Dewey, J. F., M. L. Helman, E. Turco, D. H. W. Hutton, and S. D. Knott (1989), Alpine tectonics, in *Alpine Tectonics*, edited by M. P. Coward, D. Dietrich, and R. G. Park, *Geol. Soc. London, Spec. Publ.*, 45, 265–283.

Dewey, J. F., R. E. Holdsworth, and R. A. Strachan (1998), Transpression and transtension zones, *Geol. Soc. London, Spec. Publ.*, *135*, 1–14.

Dezes, P., S. Schmid, and P. A. Ziegler (2004), Evolution of the European Cenozoic rift system: Interaction of the Alpine and Pyrenean orogens with their foreland lithosphere, *Tectonophysics*, *389*, 1–33.
Ellwanger, D., U. Wielandt-Schuster, M. Franz, and T. Simon (2011), The Quaternary of the southwest German Alpine Foreland (Bodensee-Oberschwaben, Baden-Württemberg, Southwest Germany), *Quat. Sci. J.*, *60*, 306–328, doi:10.3285/eg.60.2-3.07.
Faccenna, C., C. Piromallo, A. Crespo-Blanc, L. Jolivet, and F. Rossetti (2004), Lateral slab deformation and the origin of the western Mediterranean arcs, *Tectonics*, *23*, TC1012, doi:10.1029/2002TC001488.
Funk, H., J. K. Habicht, R. Hantke, and O. A. Pfiffner (2000), Erläuterungen Blatt 1115 Säntis, in *Geologischer Atlas der Schweiz, 1:25000*, Bern, Bundesamt für Wasser und Geologie.
Gebauer, D. (1999), Alpine geochronology of the central and Western Alps: New constraints for a complex geodynamic evolution, *Schweiz. Mineral. Petrograph. Mitt.*, *79*, 191–208.
Gerdes, A., and A. Zeh (2006), Combined U-Pb and Hf isotope LA-(MC-) ICP-MS analyses of detrital zircons: Comparison with SHRIMP and new constraints for the provenance and age of an Armorican metasediment in Central Germany, *Earth Planet. Sci. Lett.*, *249*, 47–62.
Gerdes, A., and A. Zeh (2009), Zircon formation versus zircon alteration—New insights from combined U-Pb and Lu-Hf in-situ La-ICP-MS analyses of Archean zircons from the Limpopo Belt, *Chem. Geol.*, *261*, 230–243.
Giamboni, M., K. Ustaszewski, S. M. Schmid, M. E. Schumacher, and A. Wetzel (2004), Plio-Pleistocene transpressional reactivation of Paleozoic and Paleogene structures in the Rhine-Bresse transform zone (northern Switzerland and eastern France), *Int. J. Earth Sci.*, *93*, 207–223, doi:10.1007/s00531-00003-00375-00532.
Gidon, M. (1974), L'arc alpin a t'il une origine tourbillonnaire?, *C. R. Acad. Sci. Paris*, *272*, 2412–2415.
Gleissner, P., J. Glodny, and G. Franz (2007), Rb-Sr isotopic dating of pseudomorphs after lawsonite in metabasalts from the Glockner nappe, Tauern Window, Eastern Alps, *Eur. J. Mineral.*, *19*, 723–734.
Glodny, J., U. Ring, A. Kühn, P. Gleissner, and G. Franz (2005), Crystallization and very rapid exhumation of the youngest Alpine eclogites (Tauern Window, Eastern Alps) from Rb/Sr mineral assemblage analysis, *Contrib. Mineral. Petrol.*, *149*, 699–712, doi:10.1007/s00410-005-0676-5.
Glodny, J., U. Ring, and A. Kühn (2008), High-pressure metamorphism, thrusting, strike-slip and extensional shearing in the Tauern Window, Eastern Alps: All starting at the same time? *Tectonics*, *27*, TC4004, doi:10.1029/2007TC002193.
Hancock, P. L. (1985), Brittle microtectonics: Principles and practice, *J. Struct. Geol.*, *7*, 437–457.
Heller, F. (1980), Paleomagnetic evidences for late Alpine rotations of the Lepontine area, *Eclogae Geol. Helv.*, *73*, 607–618.
Hofmann, F., R. Schlatter, and M. Weh (2000), *Erläuterungen zu Blatt 97: Beggingen (LK 1011) des Geologischen Atlas der Schweiz 1:25000*, Bundesamt für Wasser und Geologie, Bern.
Houseman, G., and P. England (1986), A dynamical model of lithosphere extension and sedimentary basin formation, *J. Geophys. Res.*, *91*, 719–729, doi:10.1029/JB091iB01p00719.
Hunziker, J. C., J. Desmons, and A. J. Hurford (1986), Thirty-two years of geochronological work in the central and Western Alps: A review on seven maps, *Mém. Géol. Lausanne*, *13*.
Illies, J. H. (1975), Recent and paleo-intraplate tectonics in stable Europe and the Rhinegraben rift system, *Tectonophysics*, *29*, 251–264.
Illies, J. H. (1978), Two stage Rhinegraben rifting, in *Tectonics and Geophysics of Continental Rifts*, edited by I. B. Ramberg and E. R. Neuman, pp. 63–71, Reidel, Dordrecht, Netherlands.
Illies, J. H., and G. Greiner (1978), Rhinegraben and the Alpine system, *Bull. Geol. Soc. Am.*, *85*, 770–782.
Keller, J. (1984), Der Jungtertiäre Vulkanismus Südwestdeutschlands: Exkursionen im Kaiserstuhl und Hegau, *Fortschr. Miner.*, *62*, 2–35.
Lacombe, O., and L. Jolivet (2005), Structural and kinematic relationships between Corsica and the Pyrenees-Provence domain at the time of the Pyreneen orogeny, *Tectonics*, *24*, TC1003, doi:10.1029/2004TC001673.
Lacombe, O., J. Anglelier, D. Byrne, and J. M. Dupin (1993), Eocene-Oligocene tectonics and kinematics of the Rhine-Saone continental transform zone, *Tectonics*, *12*, 874–888, doi:10.1029/93TC00233.
Laubscher, H. (1991), The arc of the Western Alps today, *Eclog. Geol. Helv.*, *84*, 631–659.
Laubscher, H. P. (1983), The late Alpine (Periadriatic) intrusions and the insubric line, *Mem. Soc. Geol. Ital.*, *26*, 21–30.
Lonergan, L., and N. White (1997), Origin of the Betic-Rif mountain belt, *Tectonics*, *16*, 504–522, doi:10.1029/96TC03937.
Lowrie, W., and W. Alvarez (1975), Paleomagnetic evidence for the rotation of Italy, *J. Geophys. Res.*, *80*, 1579–1592, doi:10.1029/JB080i011p01579.
Ludwig, K. R. (2009), Isoplot/Ex Ver 3.71: A geochronological toolkit for Microsoft Excel. Berkeley Geochronology Center Special Publication, Berkeley.
Maffione, M., F. Speranza, C. Faccenna, A. Cascella, G. Vignaroli, and L. Sagnotti (2008), A synchronous Alpine and Corsica-Sardinia rotation, *J. Geophys. Res.*, *113*, B03104, doi:10.1029/2007JB005214.
Mancktelow, N. (1985), The Simplon Line: A major displacement zone in the Western Lepontine Alps, *Eclog. Geol. Helv.*, *78*, 73–96.
Mardia, K. V. (1972), *Statistics of Directional Data*, Academic Press, London.
Marrett, R., and R. W. Allmendinger (1990), Kinematic analysis of fault-slip data, *J. Struct. Geol.*, *12*, 973–986.
Maurel, O., M. Brunel, and P. Monie (2002), Exhumation Cenozoıque des massifs du Canigou et de Mont-Louis (Pyrenees Orientales, France), *C. R. Geosci.*, *334*, 941–948.
Ménard, G. (1988), *Structure et cine´atique d'une chaıne de collision: Les Alpes occidentales et centrales, these de Doctorat d'Etat*, pp. 278, Univ. Joseph Fourier, Grenoble, France.
Merle, O., and L. Michon (2001), The formation of the west-European Rift: A new model exemplified by the Massif Central area, *Bull. Soc. Geol. Fr.*, *172*, 213–221.
Merle, O., P. R. Cobbold, and S. M. Schmid (1989), Tertiary kinematics in the Lepontine dome, in *Alpine Tectonics*, edited by M. P. Coward, D. Dietrich, and R. G. Park, *Geol. Soc. London, Spec. Publ.*, 45, 324–351.
Merle, O., L. Michon, G. Camus, and A. de Goer (1998), L'extension oligoce`ne sur la transversal septentronale du rift du Massif central, *Bull. Soc. Geol. Fr.*, *109*, 615–626.
Michon, L., and O. Merle (2001), The evolution of the Massif Central rift: Spatio-temporal distribution of the volcanism, *Bull. Soc. Geol. Fr.*, *172*, 201–211.
Michon, L., R. T. van Balen, O. Merle, and H. Pagnier (2003), The Cenozoic evolution of the Roer Valley rift system integrated at a European scale, *Tectonophysics*, *367*, 101–126.
Miller, K. G., G. S. Mountain, J. D. Wright, and J. V. Browning (2011), A 180-million-year record of sea level and ice volume variations from continental margin and deep-sea isotopic records, *Oceanography*, *24*, 40–53, doi:10.5670/oceanog.2011.26.
Molnar, P. (2015), Gravitational instability of mantle lithosphere and core complexes, *Tectonics*, *34*, 478–487, doi:10.1002/2014TC003808.
Morillon, A. C. (1997), Etude thermo-chronometrique appliquee aux exhumations en contexte orogenique: Le Massif des Maures (France), et les Cordilleres Betiques (Espagne), PhD thesis, 303 pp., Univ. de Nice, France.

Müller, B., V. Wehrle, H. Zeyen, and K. Fuchs (1997), Short-scale variations of tectonic regimes in the western European stress province north of the Alps and Pyrenees, *Tectonophysics*, *275*, 199–219.
Nievergelt, P., M. Liniger, N. Froitzheim, and R. Mählmann (1996), Early to mid Tertiary crustal extension in the central Alps: The Turba mylonite zone (eastern Switzerland), *Tectonics*, *15*, 329–340, doi:10.1029/93TC02312.
Oberhauser, R. (1965), Zur Geologie der West-Ostalpen-Grenzzone in Vorarlberg und im Prätigau unter besonderer Berücksichtigung der tektonischen Lagebeziehungen, *Z. Deutsch, Geol. Ges.*, *116*, 440–446.
Oberhauser, R. (2005), Zur Geologie der Staufenspitz-Gruppe südlich Dornbirn, *Forschen Entdecken*, *16*, 109–152.
Oberhauser, R., and W. Rataj (1998), Geologisch–Tektonische Übersichtskarte von Vorarlberg 1:200 000 Geologische Bundesanstalt und Vorarlberger Landesmuseumsverein.
Ortner, H., S. Aichholzer, M. Zerlauth, R. Pilser, and B. Fügenschuh (2015), Geometry, amount, and sequence of thrusting in the Subalpine Molasse of western Austria and southern Germany, European Alps, *Tectonics*, *34*, 1–30, doi:10.1002/2014TC003550.
Petit, J.-P. (1987), Criteria for the sense of movement on fault surfaces in brittle rocks, *J. Struct. Geol.*, *9*, 597–608.
Platt, J. P. (1986), Dynamics of orogenic wedges and the uplift of high-pressure metamorphic rocks, *Geol. Soc. Am. Bull.*, *97*, 1037–1053.
Platt, J. P., J. H. Behrmann, P. C. Cunningham, S. Wallis, and P. J. Western (1993), Kinematics of the Alpine arc and the motion history of Adria, *Nature*, *337*, 158–161.
Plenefisch, T., and K.-P. Bonjer (1997), The stress field in the Rhine Graben area inferred from earthquake focal mechanisms and estimations of frictional parameters, *Tectonophysics*, *275*, 71–97.
Pomella, H., H. Ortner, M. Zerlauth, and B. Fügenschuh (2015), The Alpine nappe stack in western Austria: A crustal-scale cross section, *Int. J. Earth Sci.*, *104*, 733–745.
Preusser, F., H. R. Graf, O. Keller, E. Krayss, and C. Schlüchter (2011), Quaternary glaciation history of northern Switzerland, *Quat. Sci. J.*, *60*, 282–305, doi:10.3285/eg.60.2-3.06.
Ratschbacher, L., W. Frisch, H.-G. Linzer, and O. Merle (1991), Lateral extrusion in the Eastern Alps, Part 2: Structural analysis, *Tectonics*, *10*, 257–271, doi:10.1029/90TC02623.
Reddy, S. M., J. Wheeler, and R. A. Cliff (1999), The geometry and timing of orogenic extension: An example from the Western Italian Alps, *J. Met. Geol.*, *17*, 573–589.
Ring, U. (1992), An Alpine kinematical analysis of the Penninic nappes east of the Lepontine dome: Implications for the evolution of the central Alps, *Tectonics*, *11*, 1139–1158, doi:10.1029/92TC00616.
Ring, U. (1994), The kinematics of the late Alpine Muretto fault and its relation to eastward extension and to displacement at the Engadine and Periadriatic lines, *Eclog. Geol. Helv.*, *87*, 811–831.
Ring, U. (2008), The tectonic evolution of the Franciscan Subduction Complex: Implications for the exhumation of high-pressure rocks in subduction-related accretionary wedges, *Geol. Soc. Am. Spec. Pap.*, *445*, 1–61, doi:10.1130/2008.2445.
Ring, U., J. Glodny, S. Thomson, and T. Will (2010), The Hellenic subduction system: High-pressure metamorphism, exhumation, normal faulting and large-scale extension, *Annu. Rev. Earth Planet. Sci.*, *38*, 45–76, doi:10.1146/annurev.earth.050708.170910.
Roca, E., M. Sans, L. Cabrera, and M. Marzo (1999), Oligocene to middle Miocene evolution of the central Catalan margin (northwestern Mediterranean), *Tectonophysics*, *315*, 209–233.
Rosenbaum, G., G. S. Lister, and C. Duboz (2002), Reconstruction of the tectonic evolution of the western Mediterranean since the Oligocene, *J. Virt. Expl.*, *8*, 107–130.
Rosseti, F., C. Faccenna, B. Goffé, P. Monié, A. Argentieri, R. Funiciello, and M. Mattei (2001), Alpine structural and metamorphic signature of the Sila Piccola Massif nappe stack (Calabria, Italy): Insights for the tectonic evolution of the Calabrian Arc, *Tectonics*, *20*, 112–133, doi:10.1029/2000TC900027.
Royden, L. H. (1993), Evolution of retreating subduction boundaries formed during continental collision, *Tectonics*, *12*, 629–638, doi:10.1029/92TC02641.
Sala, P., O. A. Pfiffner, and M. Frehner (2014), The Alpstein in three dimensions: Fold-and-thrust belt visualization in the Helvetic zone, eastern Switzerland, *Swiss J. Geosci.*, *107*, 177–195.
Sanderson, D. J., and W. R. D. Marchini (1984), Transpression, *J. Struct. Geol.*, *6*, 449–458.
Schmid, S., B. Fügenschuh, E. Kissling, and R. Schuster (2004), TRANSMED transects iv, v and vi: Three lithospheric transects across the Alps and their forelands, in *The TRANSMED Atlas: The Mediterranean Region from Crust to Mantle*, edited by W. Cavazza et al., pp. 44, Springer, Berlin.
Schreiner, A. (1975), Zur Frage der tektonischen oder glazigen-fluviatilen Entstehung des Bodensees, *Jber. Mitt. Oberrh. Geol. Ver., NF*, *57*, 61–75.
Schreiner, A. (1979), Zur Entstehung des Bodenseebeckens, *Eiszeitalter Ggw.*, *29*, 71–76.
Schumacher, M. E. (2002), Upper Rhine Graben: Role of preexisting structures during rift evolution, *Tectonics*, *21*(1), 1006, doi:10.1029/2001TC900022.
Sengör, A. M. C. (1976), Collision of irregular continental margins: Implications for foreland deformation of Alpine-type orogens, *Geology*, *4*, 779–782.
Sengör, A. M. C., K. Burke, and J. F. Dewey (1978), Rifts at high angles to orogenic belts: Tests for their origin and the Upper Rhine Graben as an example, *Am. J. Sci.*, *278*, 24–40.
Séranne, M. (1999), The Gulf of Lion continental margin (NW Mediterranean) revisited by IBS: An overview, in *The Mediterranean Basins: Tertiary Extension Within the Alpine Orogen*, edited by B. Durand et al., *Geol. Soc. London, Spec. Publ.*, *156*, 15–36.
Sissingh, W. (1998), Comparative Tertiary stratigraphy of the Rhine Graben, Bresse Graben and Molasse basin: Correlation of Alpine foreland events, *Tectonophysics*, *300*, 249–284.
Sissingh, W. (2001), Tectonostratigraphy of the West Alpine Foreland: Correlation of Tertiary sedimentary sequences, changes in eustatic sea-level and stress regimes, *Tectonophysics*, *333*, 361–400.
Smye, A. J., M. J. Bickle, T. J. B. Holland, R. R. Parrish, and D. J. Condon (2011), Rapid formation and exhumation of the youngest Alpine eclogites: A thermal conundrum to Barrovian metamorphism, *Earth Planet.Sci. Lett.*, *306*, 193–204.
Steck, A. (2008), Tectonics of the Simplon massif and Lepontine gneiss dome: Deformation structures due to collision between the underthrusting European plate and the Adriatic indenter, *Swiss J. Geosci.*, *101*, 515–546.
Sue, C., and P. Tricart (2002), Widespread post-nappe normal faulting in the internal Western Alps: New constraints on arc dynamics, *J. Geol. Soc. Lond.*, *159*, 61–70.
Thomas, J. C., M. E. Claudel, M. Collombet, A. Chauvin, and T. Dumont (1999), First paleomagnetic data from the sedimentary cover of the French Penninic Alps: Evidence for tertiary counterclockwise rotations in the Western Alps, *Earth Planet. Sci. Lett.*, *171*, 561–574.
Ustaszewski, K., and S. M. Schmid (2007), Latest Pliocene to recent thick-skinned tectonics at the Upper Rhine Graben-Jura Mountains junction, *Swiss J. Geosci.*, *100*, 293–312.

van Hinsbergen, D. J. J., R. L. M. Vissers, and W. Spakman (2014), Origin and consequences of western Mediterranean subduction, rollback, and slab segmentation, *Tectonics*, *33*, 393–419, doi:10.1002/tect.20125.

Vialon, P., P. Rochette, and G. Menard (1989), Indentations and rotations in the Western Alpine arc, in *Alpine Tectonics*, edited by M. P. Coward, D. Dietrich, and R. G. Park, *Geol. Soc. London, Spec. Publ.*, *45*, 189–210.

Zarki-Jakni, B., P. van der Beek, G. Poupeau, M. Sosson, E. Labrin, P. Rossi, and J. Ferrandini (2004), Cenozoic denudation of Corsica in response to Ligurian and Tyrrhenian extension: Results from apatite fission track thermochronology, *Tectonics*, *23*, TC1003, doi:10.1029/2003TC001535.

Ziegler, P. A. (1994), Cenozoic rift of western and central Europe: An overview, *Geol. Mijnbouw*, *73*, 99–127.